

Reverberation Mapping Measurements of Black Hole Masses in Six Local Seyfert Galaxies

K. D. Denney¹, B. M. Peterson^{1,2}, R. W. Pogge^{1,2}, A. Adair³, D. W. Atlee¹, K. Au-Yong³,
M. C. Bentz^{1,4,5}, J. C. Bird¹, D. J. Brokofsky^{6,7}, E. Chisholm³, M. L. Comins^{1,8},
M. Dietrich¹, V. T. Doroshenko^{9,10,11}, J. D. Eastman¹, Y. S. Efimov¹⁰, S. Ewald³,
S. Ferbey³, C. M. Gaskell^{6,12}, C. H. Hedrick^{6,8}, K. Jackson³, S. A. Klimanov^{10,11},
E. S. Klimek^{6,13}, A. K. Kruse^{6,14}, A. L  deroute³, J. B. Lamb¹⁵, K. Leighly¹⁶, T. Minezaki¹⁷,
S. V. Nazarov^{10,11}, C. A. Onken^{18,19}, E. A. Petersen⁶, P. Peterson²⁰, S. Poindexter¹,
Y. Sakata²¹, K. J. Schlesinger¹, S. G. Sergeev^{10,11}, N. Skolski³, L. Stieglitz³, J. J. Tobin¹⁵,
C. Unterborn¹, M. Vestergaard^{22,23}, A. E. Watkins⁶, L. C. Watson¹, and Y. Yoshii¹⁷

¹Department of Astronomy, The Ohio State University, 140 West 18th Avenue, Columbus, OH 43210, USA; denney@astronomy.ohio-state.edu

²Center for Cosmology and AstroParticle Physics, The Ohio State University, 191 West Woodruff Avenue, Columbus, OH 43210, USA

³Centre of the Universe, Herzberg Institute of Astrophysics, National Research Council of Canada, 5071 West Saanich Road, Victoria, BC V9E 2E7, Canada

⁴Present address: Department of Physics and Astronomy, 4129 Frederick Reines Hall, University of California at Irvine, Irvine, CA 92697-4575, USA

⁵Hubble Fellow

⁶Department of Physics & Astronomy, University of Nebraska, Lincoln, NE 68588-0111, USA.

⁷Deceased, 2008 September 13

⁸Current address: Astronomy and Astrophysics Department, Pennsylvania State University, 525 Davey Laboratory, University Park, PA 16802, USA

⁹Crimean Laboratory of the Sternberg Astronomical Institute, p/o Nauchny, 98409 Crimea, Ukraine

¹⁰Crimean Astrophysical Observatory, p/o Nauchny, 98409 Crimea, Ukraine

¹¹Isaac Newton Institute of Chile, Crimean Branch, Ukraine

¹²Current address: Astronomy Department, University of Texas, Austin, TX 78712-0259, USA

¹³Current address: Astronomy Department, MSC 4500, New Mexico State University, PO BOX 30001, La Cruces, NM 88003-8001, USA

¹⁴Current address: Physics Department, University of Wisconsin-Madison, 1150 University Avenue, Madison, WI 53706-1390, USA

¹⁵Department of Astronomy, University of Michigan, 500 Church St., Ann Arbor, MI 48109-1040, USA

¹⁶Homer L. Dodge Department of Physics and Astronomy, The University of Oklahoma, 440 W. Brooks St., Norman, OK 73019, USA

¹⁷Institute of Astronomy, School of Science, University of Tokyo, 2-21-1 Osawa, Mitaka, Tokyo 181-0015, Japan

¹⁸Plaskett Fellow; Dominion Astrophysical Observatory, Herzberg Institute of Astrophysics, National Research Council of Canada, 5071 West Saanich Road, Victoria, BC V9E 2E7, Canada

¹⁹Current address: Mount Stromlo Observatory, Research School of Astronomy & Astrophysics, The Australian National University, Cotter Road, Weston Creek, ACT 2611, Australia

²⁰Ohio University, Department of Physics and Astronomy, Athens, OH 45701-2979, USA

²¹Department of Astronomy, School of Science, University of Tokyo, 7-3-1 Hongo, Bunkyo-ku, Tokyo 113-0013, Japan

²²Steward Observatory, The University of Arizona, 933 North Cherry Avenue, Tucson, AZ 85721, USA

ABSTRACT

We present the final results from a high sampling rate, multi-month, spectrophotometric reverberation mapping campaign undertaken to obtain either new or improved $H\beta$ reverberation lag measurements for several relatively low-luminosity AGNs. We have reliably measured the time delay between variations in the continuum and $H\beta$ emission line in six local Seyfert 1 galaxies. These measurements are used to calculate the mass of the supermassive black hole at the center of each of these AGNs. We place our results in context to the most current calibration of the broad-line region (BLR) $R_{\text{BLR}}-L$ relationship, where our results remove outliers and reduce the scatter at the low-luminosity end of this relationship. We also present velocity-resolved $H\beta$ time delay measurements for our complete sample, though the clearest velocity-resolved kinematic signatures have already been published.

Subject headings: galaxies: active — galaxies: nuclei — galaxies: Seyfert

1. INTRODUCTION

The technique of reverberation mapping (Blandford & McKee 1982; Peterson 1993) has been used to directly measure black hole masses in relatively local broad-line (Type 1) AGNs for over two decades (see compilation by Peterson et al. 2004). In recent years, these measurements have become particularly desirable with the increasingly strong evidence (both observational and theoretical) that there is a connection between supermassive black hole (BH) growth and galaxy evolution (e.g., Silk & Rees 1998; Kormendy & Gebhardt 2001; Häring & Rix 2004; Di Matteo et al. 2005; Bennert et al. 2008; Somerville et al. 2008; Hopkins & Hernquist 2009; Shankar et al. 2009). Empirical relationships have been discovered for both quiescent and active galaxies that show similar correlations between the central BH and properties of the bulge of the host galaxy (well outside the gravitational sphere of influence of the black hole). Examples include correlations between the BH mass and total luminosity of stars in the galactic bulge — the $M_{\text{BH}}-L_{\text{bulge}}$ relationship (Kormendy & Richstone 1995; Magorrian et al. 1998; Wandel 2002; Graham 2007; Bentz et al. 2009a) — and between BH mass and the bulge stellar velocity dispersion — the $M_{\text{BH}}-\sigma_*$ relationship (Ferrarese & Merritt 2000; Gebhardt et al. 2000a,b; Ferrarese et al. 2001; Tremaine et al. 2002; Onken et al. 2004; Nelson et al. 2004).

²³Dark Cosmology Centre, Niels Bohr Institute, Copenhagen University

The current thrust to better understand this BH-galaxy connection relies on mass measurements of large samples of black holes in both the local and distant Universe. The masses of BHs in distant galaxies can only be measured indirectly using the scaling relationships mentioned above, as well as the AGN $R_{\text{BLR}}-L$ relationship (Kaspi et al. 2000, 2005; Bentz et al. 2006, 2009b), which provides the capability to estimate BH masses from a single spectrum of an AGN (Wandel et al. 1999). In order to understand the evolution of BH and galaxy growth over cosmological times, it is useful to compare the location of distant galaxies on these relationships with local samples. This can only be done by calibrating the local relation with direct BH mass measurements.

Local masses are measured directly in quiescent galaxies using dynamical methods (see Kormendy & Richstone 1995; Kormendy & Gebhardt 2001; Ferrarese & Ford 2005, for reviews) that rely on resolving the motions of gas and stars within the sphere of influence of the central BH and are thus very resolution intensive and only applicable in the nearby Universe. Direct measurements can also be made from observations of megamasers sometimes seen in Type 2 AGNs, but making these observations relies on a particular viewing angle into the nuclear region of these galaxies and is thus not applicable to large numbers of objects. Direct mass measurements can also be made in Type 1 AGNs using reverberation mapping, which is a method that relies on time resolution to trace the light-travel time delay between continuum and broad emission-line flux variations to measure the characteristic size of the broad line region (BLR). Using virial arguments, this size is related to the black hole mass through the velocity dispersion of the BLR gas, determined from the broad emission-line width. Although reverberation mapping is technically applicable at all redshifts, the reverberation time-delay scales with the AGN luminosity (i.e., the $R_{\text{BLR}}-L$ relationship), and this coupled with time dilation effects make it difficult and particularly time-consuming to make such measurements out to high redshift (see Kaspi et al. 2007).

The constraints for making direct BH mass measurements at large distances make the use of the $R_{\text{BLR}}-L$ relationship particularly attractive for obtaining even indirect mass estimates at all redshifts for which a broad-line AGN spectrum can be obtained. In addition, masses can be estimated for large samples of objects (e.g., McLure & Dunlop 2004; Kollmeier et al. 2006; Salviander et al. 2007; Shen et al. 2008; Vestergaard et al. 2008), facilitating studies of the BH-galaxy connection and its evolution across cosmic time (e.g., Salviander et al. 2007; Vestergaard & Osmer 2009). However, in order to reliably apply these relationships to high redshift objects and determine any evolution in the relationships themselves, local versions of the relationships need to be well-populated with high-quality data, so that calibration of these local relationships is secure (i.e., observational scatter minimized) and any intrinsic scatter is well characterized (see, e.g., Bentz et al. 2006, 2009a,b; Graham 2007; Gültekin et al. 2009; Woo et al. 2010, for recent efforts to improve scaling

relation calibration and characterization of intrinsic scatter). Furthermore, systematic uncertainties also need to be understood and minimized so that the local relations, on which all other related studies are based, are as robust as possible. For instance, systematic uncertainties are present in the direct, dynamical mass measurements of the BHs in quiescent galaxies due to model-dependencies of the mass derivation (e.g., Gebhardt & Thomas 2009 find more than a factor of two difference in the measured BH mass in M87 when they include a dark matter halo in their model; see also Shen & Gebhardt 2010 and van den Bosch & de Zeeuw 2010 for more recent model-dependent changes made to previously measured quiescent black hole masses that change the masses by similar amounts, i.e., factors of ~ 2). On the other hand, the reverberation-based masses as we present them (measuring simply the mean BLR radius from the reverberation time-delay) do not rely on any physical models; instead, the largest systematic uncertainty comes from the additional zero-point calibration of the mass scale (Woo et al. 2010). This calibration is needed due to a number of uncertainties, such as the relationship between the line-of-sight (LOS) velocity dispersion measured from the broad-line width and the actual velocity dispersion of the BLR, systematic effects in determining the effective radius, and the role of non-gravitational forces.

In this work, we present new reverberation-mapping measurements of the BLR radius and black hole mass for several nearby Seyfert galaxies from an intensive spectroscopic and photometric monitoring program. The goals of this program are (1) to improve the calibration of local scaling relationships by populating them with not only additional high-quality measurements, but also replace previous measurements of either poor quality or that were suspect for one reason or another, and (2) to take the method of reverberation mapping one step past its currently successful application of measuring BLR radii and BH masses to uncover velocity-resolved structure in the reverberation delays from the $H\beta$ emission line. This velocity-resolved analysis is a first step towards recovering velocity-dependent $H\beta$ transfer functions, or “velocity–delay maps”, which describe the response of the emission-line to an outburst from the ionizing continuum as a function of LOS velocity and light-travel time-delay (for a tutorial, see Peterson 2001; Horne et al. 2004). Creation of velocity–delay maps provides valuable knowledge of the structure, inclination, and kinematics of the BLR, which in turn will reduce systematic uncertainties in reverberation-based black hole mass measurements.

Our monitoring program spanned more than four months, over which primary spectroscopic observations were obtained nightly (weather permitting) for the first three months at MDM Observatory. Supplementary observations were gathered from other observatories around the world. Objects in our sample were targeted because (a) they had short enough expected lags (i.e., low enough luminosity) that we were likely to see sufficient variability over the course of our ~ 3 –4 month campaign to securely measure a reverberation time delay,

(b) they appeared as outliers on AGN scaling relationships and/or had large uncertainties associated with previous results due to suspected undersampling or other complications, and (c) previous observations demonstrated the potential for our high sampling-rate observations to uncover a velocity-resolved line response to the continuum variations. We also note that some of the AGNs observed in this program are among the closest AGNs and are therefore the best candidates for measuring the central black hole masses by other direct methods such as modeling of stellar or gas dynamics, which will allow a direct comparison of mass measurements from multiple independent techniques. This paper is arranged such that we present our observations and analysis in Section 2, the black hole mass measurements are described in Section 3, any velocity-resolved structures that we uncovered are presented in Section 4, and our results are discussed in Section 5.

2. Observations and Data Analysis

Except where noted, data acquisition and analysis practices employed here follow closely those laid out by Denney et al. (2009b) for the first results from this campaign on NGC 4051. The reader is also referred to similar previous works, such as Denney et al. (2006) and Peterson et al. (2004), for additional details and discussions on these practices. Throughout this work, we assume the following cosmology: $\Omega_m = 0.3$, $\Omega_\Lambda = 0.70$, and $H_0 = 70 \text{ km sec}^{-1} \text{ Mpc}^{-1}$.

2.1. Spectroscopy

Spectra of the nuclear region of our complete¹ sample (see Table 1) were obtained daily (weather permitting) over 89 consecutive nights in Spring 2007 with the 1.3 m McGraw–Hill telescope at MDM Observatory, and supplemental spectroscopic observations of most targets were obtained with the 2.6 m Shajn telescope of the Crimean Astrophysical Observatory (CrAO) and/or the Plaskett 1.8 m telescope at Dominion Astrophysical Observatory (DAO) to extend the total campaign duration to ~ 120 nights. We used the Boller and Chivens CCD spectrograph at MDM with the 350 grooves/mm grating (i.e., a dispersion of 1.33 \AA/pix) to target the $\text{H}\beta \lambda 4861$ and $[\text{O III}] \lambda\lambda 4959, 5007$ emission line region of the optical spectrum. The position angle was set to 0° , with a slit width of $5''0$ projected on the sky, resulting in a

¹We also monitored MCG 08-23-067, but because this object did not vary sufficiently during our campaign, we did not complete a full reduction and analysis of the data and do not include it as part of our final, complete sample.

spectral resolution of 7.6 \AA across this spectral region. We acquired the CrAO spectra with the Nasmith spectrograph and SPEC-10 1340×100 pixel CCD. For these observations a $3''.0$ slit was utilized, with a 90° position angle. Spectral wavelength coverage for this data set was from $\sim 3800\text{--}6000 \text{ \AA}$, with a dispersion of $1.8 \text{ \AA}/\text{pix}$ and a spectral resolution of 7.5 \AA near 5100 \AA . The actual wavelength coverage is slightly greater than this, but the red and blue edges of the CCD frame are unusable due to vignetting. The DAO observations of the $H\beta$ region were obtained with the Cassegrain spectrograph and SITe-5 CCD, where the 400 grooves/mm grating results in a dispersion of $1.1 \text{ \AA}/\text{pix}$. The slit width was set to $3''.0$ with a fixed 90° position angle. This setup resulted in a resolution of 7.9 \AA around the $H\beta$ spectral region. Figure 1 shows the mean and rms spectra of our sample based on the MDM observations. Table 2 gives more detailed statistics of the spectroscopic observations obtained for each target, including number of observations, time span of observations, spectral resolution, and spectral extraction window.

A relative flux calibration of each set of spectra was performed using the χ^2 goodness of fit estimator algorithm of van Groningen & Wanders (1992) to scale relative fluxes to the $[\text{O III}] \lambda 5007$ constant narrow-line flux. This algorithm not only makes a multiplicative scaling to account for the night-to-night differences in flux in this line caused primarily by aperture affects, but it also makes slight wavelength shifts to correct for zero-point differences in the wavelength calibration and small resolution corrections to account for small variations in the line width caused by variable seeing. The best-fit calibration is found by minimizing residuals in the difference spectrum formed between each individual spectrum and the reference spectrum, which was taken to be the average of the best spectra of each object (i.e., those obtained under photometric or near-photometric conditions). Because of this multiple-component calibration method, the final, scaled $[\text{O III}] \lambda 5007$ line flux in each spectrum is not exactly the same as the reference spectrum. Instead, there is a small standard deviation in the mean line flux due to differences in data quality that averages $\sim 1.2\%$ across our sample.

2.2. Photometry

In addition to spectral observations, we obtained supplemental V -band photometry from the 2.0 m Multicolor Active Galactic Nuclei Monitoring (MAGNUM) telescope at the Haleakala Observatories in Hawaii, the 70 cm telescope of the CrAO, and the 0.4 m telescope of the University of Nebraska. The number of observations obtained from each telescope and the time span over which observations were made of each target are given in Table 3.

The MAGNUM observations were made with the multicolor imaging photometer (MIP)

as described by Kobayashi et al. (1998a,b), Yoshii (2002), and Kobayashi et al. (2004). Photometric fluxes were measured within an aperture with radius $8''.3$. Reduction of these observations was similar to that described for other sources by Minezaki et al. (2004) and Suganuma et al. (2006), except the host-galaxy contribution to the flux within the aperture was not subtracted and the filter color term was not corrected because these photometric data were later scaled to the MDM continuum light curves (as described below). Also, minor corrections (of order 0.01 mag or less) due to the seeing dependence of the host-galaxy flux were ignored.

The CrAO photometric observations were collected with the AP7p CCD mounted at the prime focus of the 70 cm telescope ($f = 282$ cm). In this setup, the 512×512 pixels of the CCD field projects to a $15' \times 15'$ field of view. Photometric fluxes were measured within an aperture diameter of $15''.0$. For further details of the CrAO V -band observations and reduction, see the similar analysis described by Sergeev et al. (2005).

The University of Nebraska observations were conducted by taking and separately measuring a large number of one-minute images (~ 20). Details of the observing and reduction procedure are as described by Klimek et al. (2004). Comparison star magnitudes were calibrated following Doroshenko et al. (2005a,b) and Chonis & Gaskell (2008). To minimize the effects of variations in the image quality, fluxes were measured through an aperture of radius $8''.0$. The errors given for each night are the errors in the means.

2.3. Light Curves

Except where noted below for individual objects, continuum and $H\beta$ light curves were created as followed. Continuum light curves for each object were made with the V -band photometric observations and the average continuum flux density measured from spectroscopic observations over the spectral ranges listed in Table 2 (i.e., rest frame ~ 5100 Å). Continuum light curves from each source were scaled to the same flux scale following the procedure described by Denney et al. (2009b). Figure 2 (top panels) shows these merged light curves, where measurements from each different observatory are shown by the different symbols described in the figure caption.

Light curves of the $H\beta$ flux were made by integrating the line flux above a linearly interpolated continuum, locally defined by regions just blueward and redward of the $H\beta$ emission line. The $H\beta$ emission line was defined between the observed frame wavelength ranges given for each object in Table 2. The $H\beta$ light curves formed from each separate spectroscopic data set (i.e., MDM, CrAO, and DAO) were placed on the same flux scale

(i.e., that of the MDM observations) by again following the scaling procedures described by Denney et al. (2009b). An additional flux calibration step was used for NGC 3516, however, because it has a particularly extended [O III] narrow-line emission region. In an attempt to decrease the uncertainties in our relative flux calibration from slit losses of this extended emission, we made an additional correction to each MDM $H\beta$ flux measurement to account for possible differences in the observed [O III] $\lambda 5007$ flux due to seeing effects. To measure the expected differences in [O III] $\lambda 5007$ flux entering the slit as a result of changes in the nightly seeing, we followed the procedure of Wanders et al. (1992), using their artificially seeing-degraded narrow-band image of the [O III] $\lambda 5007$ emission from the nuclear region of NGC 3516 (details regarding the narrow-band data are described by Wanders et al.). Using the differences in measured flux, we scaled our MDM flux measurements accordingly. We could only do this for the MDM measurements, since we do not have accurate seeing estimates for the CrAO and DAO data sets. Because of our deliberately large aperture (see Table 2, Column 8), the effect was not appreciable for most observations, and there is no indication that our inability to complete the same analysis for the CrAO and DAO data had any measurable effect on the subsequent time-series analysis. The lower panels of Figure 2 show the $H\beta$ light curves for each object after merging the separate data sets into a single $H\beta$ light curve.

Before completing the time-series analysis, the light curves shown in Figure 2 were modified in the following ways:

1. An absolute flux calibration was applied to both continuum and $H\beta$ light curves by scaling to the absolute flux of the [O III] $\lambda 5007$ emission line given for each object in Column 3 of Table 4. For objects in which there was not a previously reported absolute flux, we calculated one from the average line flux measured from only those observations obtained at MDM under photometric conditions.
2. The host galaxy starlight contribution to the continuum flux was subtracted. This contribution, listed for each target in Column 5 of Table 4, was determined using the methods of Bentz et al. (2009b) for all objects except Mrk 290, which had not been targeted for reverberation mapping prior to our observing campaign². For Mrk 290, we use an estimate made from the spectral decomposition (following decomposition method “B” described by Denney et al. 2009a) of an independent spectrum taken at MDM with nearly the same setup as our campaign observations but covering optical

²The 2008 LAMP campaign (Bentz et al. 2009c) subsequently monitored Mrk 290, and it is currently being targeted for *HST* observations (GO 11662, PI Bentz) to measure its host starlight contribution, but the observations have not yet been completed.

wavelengths from 3500–7150 Å with a 1''5 slit. This value is only a lower limit, however, since this slit width was smaller than that of our campaign observations (i.e., 5''0).

3. We “detrended” any light curves in which we detected long-term secular variability over the duration of the campaign that is not associated with reverberation variations (Welsh 1999; see also Sergeev et al. 2007, who show that there is little correlation between long-term continuum variability and $H\beta$ line properties, demonstrating the independence of this variability on reverberation processes). Detrending is important because if the time series contains long-term trends (i.e., compared to reverberation timescales), the flux measurements are not randomly distributed about the mean and are, thus, highly correlated on these long timescales. These long time scale correlations then dominate the results of the cross correlation analysis that determines the time delay, biasing the desired correlation due to reverberation. Welsh (1999) strongly recommends removing these low-frequency trends with low order polynomials (a linear fit at the very least) to improve the reliability of cross correlation lag determinations. We took a conservative approach and only linearly detrended light curves in which there was evidence for secular variability and for which the cross correlation analysis was improved upon detrending: both light curves from Mrk 290, the $H\beta$ light curve from Mrk 817, and the continuum light curve from NGC 3227 (see Section 2.4 for further discussion). These fits are shown in Figure 2 for each of these respective light curves. It was unnecessary to detrend all light curves, as no improvement in the cross correlation analysis would result from detrending light curves that already have a relatively flat mean flux. Also, it is not surprising for associated continuum and line light curves to exhibit different long-term secular trends, since the relationship between the measured continuum and the ionizing continuum responsible for producing the emission lines may not be a linear one (Peterson et al. 2002), and the exact response of the line depends on the detailed structure and dynamics of the BLR.
4. We excluded the points from the Mrk 817 light curve with $JD < 2454200$ because (1) there is a large gap in the data between these points and the rest of the light curve, and (2) there is little to no coherent variability pattern seen here (i.e., the continuum is relatively flat and noisy, and the $H\beta$ fluxes are particularly noisy and are of otherwise little use, given there are no continuum points at earlier times).

Tabulated continuum and $H\beta$ fluxes for all objects, except for NGC 4051 which were previously reported by Denney et al. (2009b), are given in Tables 5 and 6, respectively. Values listed represent the flux of each observation after completing all flux calibrations described above (i.e., absolute flux calibration based on the $[O III] \lambda 5007$ emission-line flux and host galaxy starlight subtraction), but before detrending, since this results in an arbitrary

flux scale normalized to 1.0. The final calibrated light curves used for the subsequent time-series analysis are shown for each object in the left panels of Figure 3. Statistical parameters describing these calibrated light curves (again, before detrending) are given in Table 7, where Column (1) lists each object. Columns (2) and (3) are mean and median sampling intervals, respectively, between data points in the continuum light curves. The mean continuum flux is shown in column (4), while column (5) gives the excess variance, calculated as

$$F_{\text{var}} = \frac{\sqrt{\sigma^2 - \delta^2}}{\langle f \rangle} \quad (1)$$

where σ^2 is the variance of the observed fluxes, δ^2 is their mean square uncertainty, and $\langle f \rangle$ is the mean of the observed fluxes. Column (6) is the ratio of the maximum to minimum flux in the continuum light curves. Columns (7–11) display the same quantities as Columns (2–6) but for the H β light curves.

2.4. Time-Series Analysis

We performed a cross correlation analysis to evaluate the mean light-travel time delay, or lag, between the continuum and H β emission line flux variations. We primarily employed an interpolation scheme (Gaskell & Sparke 1986; Gaskell & Peterson 1987, with the modifications of White & Peterson 1994). Using this method, we first interpolate (with an interval equal to roughly half the median data spacing, i.e., ~ 0.5 day) between points in the emission-line light curve before cross correlating it with the original continuum light curve, calculating cross correlation coefficients, r , for many potential lag values (both positive and negative). We then average these cross correlation coefficients with those measured by imposing the same set of possible lag values in the case where we cross correlate an interpolated continuum light curve with the original emission-line light curve. This gives us a distribution of average cross correlation coefficients as a function of possible lags, known as the cross correlation function (CCF). We checked the results from this method with the discrete correlation method of Edelson & Krolik (1988), also employing the modifications of White & Peterson (1994), but we do not show these results here, since they are consistent with our primary cross correlation method, and provide no additional information.

The right panels of Figure 3 show the adopted cross correlation results for each object (i.e., after detrending selected light curves; see below for a discussion of the effect of detrending on this analysis). Here, the auto-correlation function (ACF), computed by cross correlating the continuum with itself, is shown in the top right panel for each object, and the CCF computed by cross correlating the H β light curve with that of the continuum, is shown

in the bottom right. Because the CCF is a convolution of the transfer function with the ACF, it is instructive to compare the two distributions, as the lag measured through this type of cross correlation analysis will depend not only on the delay map, but also on characteristic time scales of the continuum variations (see, e.g., Netzer & Maoz 1990). We characterize the time delay between the continuum and emission-line variations by the parameter τ_{cent} , the centroid of the CCF based on all points with $r \geq 0.8r_{\text{max}}$, as well as the lag corresponding to the peak in the CCF at $r = r_{\text{max}}$, τ_{peak} . Time dilation-corrected values of τ_{cent} and τ_{peak} were determined for each object using the redshifts listed in Table 1, i.e., $\tau_{\text{rest}} = \tau_{\text{obs}}/(1+z)$, and are given in Table 8. Uncertainties in both lag determinations are computed via model-independent Monte-Carlo simulations that employ the bootstrap method of Peterson et al. (1998), with the additional modifications of Peterson et al. (2004).

Visual inspection of the CCFs of selected objects before and after detrending was made to determine if detrending these light curves was warranted. Based on the combined properties of the light curves shown in Figure 2 (whether or not an overall slope appeared in the flux across the extent of our campaign) and the CCFs, shown in Figure 4 for Mrk 290, Mrk 817, and NGC 3227 before and after detrending, we ultimately decided to adopt the detrending for the following reasons listed for each object:

Mrk 290 — The top panels of Figure 4 show that before detrending (left), the peak of the CCF is broader than the detrended peak (right) and is blended with an aliased peak at ~ 30 days. Since the reverberation lag is clearly seen in the Mrk 290 light curves in Figures 2 and 3 and the peak of highest significance is the same both before and after detrending, the presence of this alias only acts to decrease the precision of our lag measurements. While τ_{cent} is roughly one day smaller after detrending (a difference less than even the measured uncertainty) due to the reduced significance of the aliased peak at ~ 30 days by a factor of almost 10, the detrended CCF is narrower and the measured lags more precise, so we adopt the detrended measurements.

Mrk 817 — The middle panels of Figure 4 show the original (left) and detrended (right) CCFs from the analysis of Mrk 817. The choice to detrend was marginal in this case. The process resulted in a larger observed lag ($\tau_{\text{cent}} = 14.48$ days versus $\tau_{\text{cent}} = 11.93$) after detrending, contrary to the typical expectation that lags will be underestimated after detrending (since the process removes low frequency variability). We adopt the detrended results because the resulting CCF is narrower, particularly with respect to lags $\lesssim 0.0$ days, and the resulting lag measurement is more consistent with past results that we hold to be reliable (see Section 5.1).

NGC 3227 — The bottom panels of Figure 4 show the original (left) and detrended (right)

CCFs from the analysis of NGC 3227. Here it is obvious that not detrending the light curves results in a non-physical measurement of the lag at ~ -33 days with a broad peak (due to aliasing effects between the features with the highest flux in each of the original continuum and $H\beta$ light curves). While the physical peak (i.e., with positive lag, as seen and measured from the detrended CCF) is present, every lag is of low significance, i.e., $r \lesssim 0.4$. After detrending, the CCF peak at negative lags is still present, however the 'true' reverberation signal at a lag of ~ 4 days is rightfully more significant.

3. Black Hole Masses

We assume that the motions of the BLR are dominated by the gravity of the central black hole so that the mass of the black hole can be defined by

$$M_{\text{BH}} = \frac{f c \tau (\Delta V)^2}{G}. \quad (2)$$

Here, τ is the measured emission-line time delay, so that $c\tau$ represents the BLR radius, and ΔV is the BLR velocity dispersion. The dimensionless factor f depends on the structure, kinematics, and inclination of the BLR, and we adopt the value of Onken et al. (2004), $f = 5.5 \pm 1.4$, determined empirically by adjusting the zero-point of the reverberation-based masses to scale the AGN $M_{\text{BH}}-\sigma_*$ relationship to that of quiescent galaxies.

An estimate of the BLR velocity dispersion is made from the width of the Doppler-broadened $H\beta$ emission line. This line width is commonly characterized by either the FWHM or the line dispersion, i.e., the second moment of the line profile. Table 8 gives both FWHM and line dispersion, σ_{line} , measurements from the rms spectra of all objects except Mrk 817, in which the rms profile was not well defined (see Figure 1), and thus we measured the width from the mean spectrum. All widths and their uncertainties were measured employing methods described in detail by Peterson et al. (2004). We removed the narrow-line [O III] $\lambda\lambda 4959, 5007$ emission and the narrow-line component of $H\beta$ from all objects before these line widths were measured (except for NGC 4051, where this component could not be reliably isolated due to the line profile shape and, in any case, does not affect our rms line width measurements; see Denney et al. 2009b). Flux contributions from the narrow-line component will not contaminate the line widths measured in the rms spectrum (i.e., the narrow-line component does not vary in response to the ionizing continuum on reverberation timescales), so removal of this component was generally unnecessary for most objects in our sample; however, we do so for all objects anyway to check the accuracy of our $H\beta$ to O III $\lambda 5007$ line ratio determinations (Table 4, column 4) by looking for any significant

residual narrow-line emission in the rms spectra of Figure 1. The exception to this is for Mrk 817: since we measured the width in the mean spectrum, it was necessary to remove the narrow-line before measuring the line widths because the narrow-line component will bias (i.e., underestimate) line widths measured in the mean spectrum or in any single-epoch spectrum (see Denney et al. 2009a). Also, for the width measurements in two cases, Mrk 290 and NGC 3227, we narrowed the line boundaries to 4935–5064 Å and 4810–4942 Å, respectively, compared to what was used for the flux measurements, since the rms line profiles of these objects were clearly narrower than their mean profiles (the rms profile is often narrower than the mean profile, which is not surprising, given that likely not all flux seen in the mean spectrum varies in response to the continuum; see, e.g., Korista & Goad 2004).

Black hole masses for all objects, calculated from equation (2), are listed in Table 8 and were calculated using τ_{cent} , for the time delay, τ , and the quoted line dispersion, σ_{line} , for the emission-line width, ΔV . This combination of measurements for the line width and reverberation lag is not only appropriate because it is the combination used by Onken et al. (2004) to determine the value of the scale factor, f , that we adopt here, but also because Peterson et al. (2004) show that this combination also results in the strongest virial relation between line width and BLR radius, i.e., $R \sim \Delta V^{-0.5}$. The exception to this prescription for the black hole mass calculation is Mrk 817, which has a poorly defined, triple-peaked rms line profile. Because the rms profile is weak and poorly-defined, we measure the line widths from the mean spectrum and use the Collin et al. (2006) calibration of the scale factor determined for the line dispersion measured from the mean spectrum, $f = 3.85$. Statistical and observational uncertainties have been included in these mass measurements, but intrinsic uncertainties from sources such as unknown BLR inclination cannot be accurately ascertained. We also note here that there has been some debate in the literature as to the importance of radiation pressure on black hole masses calculated using virial assumptions, since the outward radiation force has the same radial dependence as gravity (see Marconi et al. 2008; Netzer 2009; Marconi et al. 2009). As there is not yet conclusive evidence suggesting a radiation-pressure correction is important for the relatively low Eddington ratio objects we present here, we do not make this correction, but a radiation-pressure corrected mass can be computed from the observables given in Table 8 and the formulae provided by Marconi et al. (2008).

4. Velocity-Resolved Reverberation Lags

The primary cross correlation analysis presented above was intended to measure the average time delay across the full extent of the BLR from which to ascertain the mean, or

“characteristic,” radius of the $H\beta$ -emitting region of the BLR to use for calculating black hole masses. For this reason, we utilized the full line flux from which to measure the reverberation signal. However, the BLR is an extended region, and therefore, the light-travel time for the ionizing continuum to reach different volume elements within the BLR will vary across the extent of the emitting region. The expectation is then that the responding BLR gas variations will lag the continuum variations on slightly different time scales as a function of the line of sight velocity. Measuring and mapping these slight differences in the BLR response time across velocity space recovers the transfer function, which is easily visualized as a velocity–delay map (see Horne et al. 2004). Recovering an unambiguous velocity–delay map is a continuing goal of reverberation mapping analyses, as the construction and analysis of such a map is our best hope, with current technology, of gaining insight into the geometry and kinematics of the BLR.

The construction and analysis of full two-dimensional velocity–delay maps is beyond the scope of this work and remains the focus of future research. However, we do present a more simple reconstruction of the velocity-dependent reverberation signal, observed across the $H\beta$ emission line region when we divide the line flux into eight velocity-space bins of equal flux. These results for NGC 4051, NGC 3516, NGC 3227, and NGC 5548 have been previously published (Denney et al. 2009b,c) but are included again here for completeness. Line boundaries are the same as those used in the full line analysis, except where noted in Table 2. In these cases the narrowed boundaries given above for Mrk 290 were used, and a discussion of the difference in boundary choices for the other objects is presented by Denney et al. (2009c). Light curves were created from measurements of the integrated $H\beta$ flux in each bin and then cross correlated with the continuum light curve following the same procedures described above. Figure 5 shows the results of this analysis for all objects, where the top panel shows the division of each rms $H\beta$ line profile into the eight velocity bins, and the bottom panels shows the lag measurements and uncertainties for each of these bins. Error bars in the velocity direction represent the bin width. We see a variety of velocity-resolved responses that we discuss in further detail below.

5. Discussion

5.1. Comparison with Previous Results

Some of the objects in this campaign were targeted, at least in part, because they have previously appeared as outliers on AGN scaling relationships, in particular, the $R_{\text{BLR}}-L$ relationship. As such, all objects except Mrk 290 have previous reverberation results, several of which were suspect for one reason or another and warranted re-observation. Based

on the outcomes of the current analysis, we will group our results into three categories: (1) new measurements for an object never before targeted, i.e., Mrk 290, (2) replacement measurements for objects that had uncertain results (typically due to undersampling) and for which our results completely replace any previous measurements of the $H\beta$ reverberation lag, i.e., NGC 3227, NGC 3516, and NGC 4051, and (3) additional measurements of objects for which we already trust the previous lag measurements, i.e., NGC 5548 and Mrk 817. In this context, we can compare our new results to previously published results.

5.1.1. *New Measurements*

At the time of our campaign (first half of 2007), reverberation mapping had never before targeted Mrk 290. However, in 2008 LAMP also monitored Mrk 290 for a reverberation analysis (see Bentz et al. 2009c), although they were unable to recover an unambiguous reverberation lag measurement from their data because Mrk 290 exhibited little variability during their campaign. Therefore, the results we present here are the only reverberation measurements of this object.

5.1.2. *Replacement Measurements*

Our current measurements of NGC 3227, NGC 3516, and NGC 4051 should completely supersede previous results measuring a reverberation radius based on $H\beta$ and the black hole mass. A thorough comparison between our new measurement of the BLR radius of NGC 4051 and that from past studies is discussed by Denney et al. (2009b), and the reader is referred to this work for details. However, the main conclusion of that comparison is that the light curves from which previous measurements of the lag were made (e.g., Peterson et al. 2000) were undersampled, leading to an overestimate of the lag. Our current study remedied this problem with a much higher sampling rate, routinely obtaining more than one observation per day.

Previous reverberation lag measurements of the $H\beta$ -emitting region in NGC 3227 (Salamanca et al. 1994; Winge et al. 1995; Onken et al. 2003) were reanalyzed by Peterson et al. (2004). The $H\beta$ light curves of Salamanca et al. (1994) from a Lovers of Active Galaxies (LAG) campaign were undersampled, and they do not even attempt to measure a time delay from them. Winge et al. (1995) report an $H\beta$ lag of 18 ± 5 days from observations taken during a period in which the optical luminosity was only ~ 0.3 dex larger than our current observations (i.e., a change in radius of $\sim 40\%$ is expected from such a change in luminosity, based on

a $R_{\text{BLR}}-L$ relationship slope of ~ 0.5). However, their average and median sampling intervals were ~ 6 and four days, respectively, which is marginally sampled compared to what is needed for this low luminosity source. These early reverberation campaigns did not have the benefit of the predictive power that we currently have with the $R_{\text{BLR}}-L$ relationship to use for planning campaign observations; i.e., these campaigns were fundamentally exploratory. A reanalysis of the LAG consortium data presented by Salamanca et al. (1994) was conducted by Onken et al. (2003) using the van Groningen & Wanders (1992) algorithm to reduce uncertainties in the relative flux calibration of the spectra. Onken et al. found an $H\beta$ lag of $\tau_{\text{cent}} = 12.0_{-9.1}^{+26.7}$ days, consistent with the results of Winge et al. (1995). Later, Peterson et al. (2004) also re-analyzed the CTIO data presented by Winge et al. (1995) with the van Groningen & Wanders (1992) algorithm and further re-examined the LAG data rescaled by Onken et al. (2003). This reanalysis resulted in some improvement in the $H\beta$ lag determinations and uncertainties, i.e., smaller overall lags, however, the reanalyzed values still had large uncertainties, resulting in a measurement consistent with zero lag: $\tau_{\text{cent}} = 8.2_{-8.4}^{+5.1}$ days and $\tau_{\text{cent}} = 5.4_{-8.7}^{+14.1}$ days for the CTIO and LAG data sets, respectively (Peterson et al. 2004). It is clear that our new measurement of the $H\beta$ lag in NGC 3227 of $\tau_{\text{cent}} = 3.75_{-0.82}^{+0.76}$ days should supersede these past results.

Likewise, the previous reverberation data for NGC 3516 also came from a LAG consortium campaign, also with a sampling interval of ~ 4 days (Wanders et al. 1993). Since the lag for this object was at least larger than the sampling rate, the undersampling was not as severe a handicap as for other objects in our sample, such as NGC 4051 and NGC 3227. Thus, reanalysis of the LAG data first by Onken et al. (2003) and then by Peterson et al. (2004) measure lags of $\tau_{\text{cent}} = 7.3_{-2.5}^{+5.4}$ days and $\tau_{\text{cent}} = 6.7_{-3.8}^{+6.8}$ days, respectively, that are consistent with the original analysis by Wanders et al., who measure the peak $H\beta$ lag to be 7 ± 3 days, with the centroid of the CCF yielding a radius of 11 light days. All of these centroid measurements are consistent with our new measurement of $\tau_{\text{cent}} = 11.68_{-1.53}^{+1.02}$ days. Also, the LAG spectra were obtained through a narrow ($2''$) slit; as the narrow-line region in this object is partially resolved, it was necessary to make seeing-dependent corrections to the continuum and emission-line measurements (Wanders et al. 1992) that are both large and uncertain. For our new measurements, the aperture corrections are small and have a negligible effect on the final results; the seeing-corrected and uncorrected fluxes differ by, on average, $0.09 \pm 0.05\%$, which is smaller than the standard deviation of our relative flux scaling of 1.6% for NGC 3516. Clearly, our new observations with an approximately daily sampling rate show great improvement over past campaigns, for these objects, and the results presented here should supersede past values of the $H\beta$ lag measured for NGC 3227, NGC 3516, and NGC 4051.

5.1.3. Additional Measurements

The goals of this campaign were not only to re-observe outliers or objects with highly uncertain lag measurements but also to explore the possibility of uncovering velocity-resolved kinematic signatures and eventually reconstruct velocity–delay maps. Therefore, we also monitored two objects, NGC 5548 and Mrk 817, for which previous reverberation mapping results are solid, and lags measured from this campaign are simply to be considered additional measurements of the BLR radius. Reasons for making repeat reverberation measurements of AGNs include (1) exploring the radius-luminosity relationship in a single source, (2) checking the repeatability of the mass measurements for AGNs at different times, in different luminosity states, and with different line profiles, and (3) testing different characterizations of the line width (i.e., determining what line width measure leads to the most repeatable mass value). The mean lag and black hole mass results presented here for NGC 5548 are consistent with past results, taking into account the luminosity state of NGC 5548 during our campaign compared with other campaigns (i.e., NGC 5548 has been in a low luminosity state for the past several years, but the measured lags have been consistently smaller, as expected for this low state; also see Bentz et al. 2007, 2009c).

We also monitored Mrk 817, which is the highest luminosity object in our present sample. Previous measurements of the $H\beta$ radius were made by Peterson et al. (1998) from an eight-year campaign to monitor nine Seyfert 1 galaxies. From this campaign, they separately measured the lag from three different observing seasons. The reanalysis of this data by Peterson et al. (2004) resulted in rest-frame τ_{cent} measurements of $19.0^{+3.9}_{-3.7}$, $15.3^{+3.7}_{-3.5}$, and $33.6^{+6.5}_{-7.6}$ days. Bentz et al. (2009b) calculate a weighted average of $\log \tau_{\text{cent}}$ from these three measurements of (converted back to linear space) $\langle \tau_{\text{cent}} \rangle_{\text{wt}} = 21.8^{+2.4}_{-3.0}$ days at an average luminosity of $\langle \log L_{5100} \rangle_{\text{wt}} = 43.64 \pm 0.03$ to use in calibrating the $R_{\text{BLR}}-L$ relationship. The luminosity of Mrk 817 during our campaign was only about 0.1 dex higher than the weighted average luminosity quoted by Bentz et al., and our measured lag of $\tau_{\text{cent}} = 14.04^{+3.41}_{-3.47}$ days is highly consistent with the shortest lag of Peterson et al. and marginally consistent with the 19.0 day lag and the weighted average. Furthermore, the virial mass that we measure (see Column 8 of Table 8) is also consistent with those given by Peterson et al. (2004). Unfortunately, we were not able to improve on the uncertainties associated with these measurements, as our $H\beta$ light curve for this object was rather noisy (see Figures 2 and 3), which decreases the certainty with which we are able to trace the reverberated continuum variations in the line light curve. Since there was neither an improvement over nor a discrepancy with past measurements, this new result is simply added to past results as an additional measurement of the $H\beta$ -based BLR radius and M_{BH} in Mrk 817.

5.2. The BLR Radius Luminosity Relationship

To investigate the outcome of our goal to improve the calibration of scaling relations by re-examining objects that had large measurements uncertainties and/or that appeared as outliers on these scaling relationships, we place our new measurements in context to the $R_{\text{BLR}}-L$ relationship most recently calibrated by Bentz et al. (2009b). Luminosities were measured from the average, host-corrected continuum flux density measured within the 5100 Å rest-frame continuum windows listed for each object in Table 2. For most objects, we simply corrected for Galactic reddening along the line of sight (Schlegel et al. 1998); however, NGC 3227 and NGC 3516 show evidence of internal reddening that must be taken into account in determining the luminosity. Gaskell et al. (2004) argue that the UV-optical continua of AGNs are all very similar, so that the reddening can be estimated by dividing the spectrum of a reddened AGN by the spectrum of an unreddened AGN. In the case of NGC 3227, we use the value of A_B determined by Crenshaw et al. (2001) by comparing the UV-optical spectrum of NGC 3227 to the unreddened spectrum of NGC 4151. For NGC 3516, we consider two methods for estimating the reddening, which result in consistent estimates of A_B : (1) we follow the Crenshaw et al. method, comparing the spectrum of NGC 3516 again to that of NGC 4151, which results in $A_B = 1.72$, and (2) we use the Balmer decrement measured from the broad components of the $H\alpha$ and $H\beta$ emission lines to estimate a reddening of $A_B = 1.68$. These two values are highly consistent, and we adopt the average between the two methods of $A_B = 1.70$. Our measured luminosities are given in Column 9 of Table 8, where the uncertainties in the luminosities are the standard deviation in the continuum flux over the course of the campaign, except for NGC 4051, where the uncertainty in the distance is added in quadrature to this (see Denney et al. 2009b).

The top panel of Figure 6 shows the Bentz et al. (2009b) $R_{\text{BLR}}-L$ relationship, reproduced from the bottom panel of their Figure 5. Here, we have differentiated the objects targeted for our present campaign with solid squares, while all other objects presented by Bentz et al. are open squares. The bottom panel of Figure 6 shows our current results, where the objects for which our new measurements are either truly new (i.e., Mrk 290) or have become replacements for old values are shown by the solid stars, and we no longer plot the old values. Our additional measurements for NGC 5548 and Mrk 817 are shown with the open stars, and the previous weighted average lags and luminosities for these objects as reported by Bentz et al. are still present in this bottom panel. The reader should immediately notice the increased precision and accuracy of our new and replacement measurements, where it is important to note that we have *not* determined a new fit to the data³. Clearly, these

³Re-evaluating the fit to and scatter in this relationship is outside the scope of this paper but is planned

better measurements emphasize the small intrinsic scatter in this relationship, reinforcing the apparently homologous nature of AGNs, even over many orders of magnitude in luminosity. The results from this campaign also support the conclusion of Peterson (2010) that improving this relationship further will not come from simply obtaining more BLR radii measurements to “beat down” the noise, but rather, from more reliable, higher-precision measurements.

5.3. Velocity-Resolved Results

The cleanest cases of a velocity-resolved reverberation response are for NGC 3516, NGC 3227, and NGC 5548, where we see kinematic signatures indicating apparent infall, outflow, and non-radial, or “virialized,” motions, respectively. Denney et al. (2009c) discuss the velocity-resolved results for these three objects and the implications of these different kinematic signatures in the context of our overall understanding of the BLR and the use of BLR radii measurements for determining black hole masses. In addition, Denney et al. (2009b) present and discuss the marginally velocity-resolved lags shown here for NGC 4051, and so those results are not discussed further here.

The objects not discussed in previous publications are Mrk 290 and Mrk 817. Figure 5 shows that there is very little variation in the reverberation lag across the full width of the Mrk 290 line profile, indicating that any differences in the reverberation lag across the extent of the $H\beta$ -emitting region in this object were unresolvable with the sampling rate of our campaign. An additional possibility for the uniform response we observed (i.e., small range in lags and no short lags observed) could be that the highest velocity gas seen in the wings of the mean spectrum is optically thin, and therefore does not respond to the continuum variations. This is supported by the narrowness of the $H\beta$ profile in the rms spectrum compared to that observed in the mean spectrum. On the other hand, based on the relative emission-line strengths of the high-velocity wings in several AGNs, Snedden & Gaskell (2007) argue against this interpretation.

At first glance, Mrk 817 appears to show an outflow signature similar to that of NGC 3227, however, cross correlation between the continuum light curve and those derived from the line flux in the first four velocity bins actually results in lag determinations that are, though negative, largely consistent with zero lag. Ignoring these first bins gives results similar to Mrk 290, where no velocity-dependent differences in the lags are resolved. Taken at face value, this result is curious. We present binned light curves of the Mrk 817 line profile in Figure 7,

for future work that will include all new, relevant data (see, e.g., Bentz et al. 2009c).

where to increase the clarity of the discrepancy between the red and blue sides of the line for this discussion, we have combined sets of two bins to make a total of 4 bins instead of eight, i.e., we plot the flux from bin 1 added to that of bin 2, bin 3 added to bin 4, etc. For completeness we also recompute the CCFs (also shown in Fig. 7) and velocity-resolved lag measurements for these four combined bins and find results consistent with simply taking the average of the lags of each set of two bins that we combined, though the uncertainties in the newly measured lags are generally smaller, particularly for the bluest and reddest bins. Upon inspection of the individual light curves for these bins, it becomes apparent that the cross correlation analysis for these bins essentially failed, not finding a strong correlation between the continuum flux variability and that seen in the light curves of Bin 1 and Bin 2. The light curves show a lack of variability in the flux in these bins during the first half of the campaign, and then a fairly monotonic rise in flux during the second half, so the peak in the continuum flux seen near \sim JD2454230 is not seen in the light curves of Bins 1 and 2, and instead, the feature the cross correlation analysis picks up is the trough near \sim JD2454282, apparently seen in the Bins 1 and 2 light curves \sim 8–10 days earlier. This combination causes the cross correlation analysis to give unreliable results. Furthermore, no real indication of the expected positive lag can be seen by eye, as can with the other bins (and other objects, for that matter). The observations could be explained by some gas having an unresolved velocity structure near the mean radius measured for this object and there also being an outflowing component in the BLR of this object, so that the blue-shifted gas is primarily along line of sight and a resulting zero day lag is measured. However, given that (1) the overall variability observed in this object was small during this campaign, and (2) the $H\beta$ profile is very broad, leading to a small variability signal spread over a large wavelength range, we cannot make any strong conclusions at this time. Future efforts will be made both to glean further information from the velocity–delay map reconstructed from our current data as well as to re-analyze the previous monitoring data on this object in an attempt to search for any other indications of velocity-resolved signatures.

Despite the differences we see in the velocity-resolved kinematics across our sample of objects, we do not believe that there is cause for concern for the masses derived from the mean BLR radii measured from these reverberation lags. Obviously, observing unresolved, virial, or infalling gas motions certainly does not question the validity of our assumption that the BLR motions are gravitationally dominated, but indications of outflow may be more problematic. However, even given these signatures, the mean lag we measure is still consistent with lags derived from the majority of the emission-line gas. Besides, it is only gas outflowing at velocities larger than the escape velocity that would break the validity of our assumptions, and this does not seem to be the case. There are good observational and theoretical reasons to believe that there are multiple components within the BLR (e.g., disk

and wind components), and the disk-wind model of Murray et al. (1995), for example, is still able to justify the constraint of the black hole mass by the reverberation mapping radii measurements, even with the presence of a wind (see Chiang & Murray 1996).

From velocity-resolved studies such as the one discussed here and in our previous publications on this data set (Denney et al. 2009b,c), it is clear that high-cadence reverberation mapping studies are beginning to push the envelope with respect to the amount of information we are able to glean from data of high quality and homogeneity. The next goal is to attempt a reconstruction of the velocity-resolved transfer function through the production of velocity–delay maps, with priority placed on the objects shown here and discussed by Denney et al. (2009c) that exhibit statistically significant kinematic signatures of infall, outflow, and virialized motions (NGC 3516, NGC 3227, and NGC 5548, respectively). Preliminary results from this analysis show the potential to reveal the types of structured maps that will hopefully provide additional constraints on future models of the BLR and more clearly reveal distinct kinematic structures responsible for the velocity-resolved signatures we presented here.

6. Conclusion

We have reported the results for our complete sample of six local Seyfert 1 galaxies that were monitored in a reverberation mapping campaign that aimed to remeasure the BLR radius from $H\beta$ emission in objects that previously had poor measurements (large measurement uncertainties and/or undersampled light curves) or that were targeted with the aim of recovery of velocity-resolved reverberation lag signals and/or transfer functions. Based on the measured luminosities of our sample over the course of our ~ 4 month campaign, we measure $H\beta$ lags that are in excellent agreement with the expectations of the most recent calibration of the $R_{\text{BLR}}-L$ relationship of Bentz et al. (2009b).

Combining these lag measurements with velocity dispersion measurements estimated from the width of the broad $H\beta$ emission line, we make direct black hole mass measurements for our entire sample. Based on a comparison of our results with previous measurements (where available), most of our sample constitutes results that are either entirely new (Mrk 290) or supersede past measurements (NGC 3227, NGC 3516, and NGC 4051). However, for NGC 5548 and Mrk 817, we compared our current mass measurements with past results and find them consistent within the measurements uncertainties, and therefore, place these results under the category of “additional measurements” for these objects.

An additional goal of this campaign was to determine velocity-resolved reverberation

lags across the extent of the $H\beta$ -emitting region of the BLR for use in future efforts to recover velocity–delay maps to help constrain the geometry and kinematics of the BLR. Though the velocity structure in some of our targets remained unresolved on sampling-rate-limited time scales, we still found some statistically significant and kinematically diverse velocity-resolved signatures, even within this small sample. We see indications of apparent infall, outflow, and virialized motions, which, if taken at face value, would indicate that the BLR is a complicated region that differs from object to object. However, given the small scatter in the $R_{\text{BLR}}-L$ relation and the consistency with which we are able to measure the BLR radius and black hole mass in multiple objects across dynamical time scales (e.g., NGC 5548 and Mrk 817), it is unlikely that the steady-state dynamics within this region are truly this diverse. The BLR could be made up of multiple kinematic components with possible transient features such as winds and/or warped disks that travel through the line of sight to the observer over dynamical timescales. In such a scenario, evidence for different types of kinematic signatures would arise depending on the observer’s line of sight through this region at a given time. In order to quantify such possibilities and fit models to the velocity-resolved data, it is necessary to collect more velocity-resolved reverberation mapping results for these objects, as well as others. This remains a goal for future observing programs, and efforts are focused on recovering velocity–delay maps for the current sample. Similar efforts are being made by the LAMP consortium (M. Bentz, priv. comm.) with the sample presented by Bentz et al. (2009c), increasing our probability of success for this elusive goal of reverberation mapping.

We would like to thank Luis Ho for providing the optical spectra of the $H\beta$ and $H\alpha$ regions of NGC 3516 from which we calculated the Balmer decrement to determine the degree of internal reddening. We acknowledge support for this work by the National Science Foundation through grant AST-0604066 to The Ohio State University. MCB gratefully acknowledges support provided by NASA through Hubble Fellowship grant HF-51251 awarded by the Space Telescope Science Institute, which is operated by the Association of Universities for Research in Astronomy, Inc., for NASA, under contract NAS 5-26555. CMG is grateful for support by the National Science Foundation through grants AST 03-07912 and AST 08-03883. MV acknowledges financial support from HST grants HST-GO-10417, HST-AR-10691, and HST-GO-10833 awarded by the Space Telescope Science Institute, which is operated by the Association of Universities for Research in Astronomy, Inc., for NASA, under contract NAS5-26555. The Dark Cosmology Centre is funded by the Danish National Research Foundation. VTD acknowledges the support of the Russian Foundation for Basic Research (project no. 09-02-01136a) to the Crimean Laboratory of the Sternberg Astronomical Institute. SGS acknowledges support through Grant No. 5-20 of the “Cosmomicrophysics” program of the National Academy of Sciences of Ukraine to CrAO. The

CrAO CCD cameras have been purchased through the US Civilian Research and Development Foundation for the Independent States of the Former Soviet Union (CRDF) awards UP1-2116 and UP1-2549-CR-03. This research has made use of the NASA/IPAC Extragalactic Database (NED) which is operated by the Jet Propulsion Laboratory, California Institute of Technology, under contract with the National Aeronautics and Space Administration.

REFERENCES

- Bennert, N., Canalizo, G., Jungwiert, B., Stockton, A., Schweizer, F., Peng, C. Y., & Lacy, M. 2008, *ApJ*, 677, 846
- Bentz, M. C., Peterson, B. M., Netzer, H., Pogge, R. W., & Vestergaard, M. 2009a, *ApJ*, 697, 160
- Bentz, M. C., Peterson, B. M., Pogge, R. W., & Vestergaard, M. 2009b, *ApJ*, 694, L166
- Bentz, M. C., Peterson, B. M., Pogge, R. W., Vestergaard, M., & Onken, C. A. 2006, *ApJ*, 644, 133
- Bentz, M. C., et al. 2007, *ApJ*, 662, 205
- . 2009c, *ApJ*, 705, 199
- Blandford, R. D., & McKee, C. F. 1982, *ApJ*, 255, 419
- Chiang, J., & Murray, N. 1996, *ApJ*, 466, 704
- Chonis, T. S., & Gaskell, C. M. 2008, *AJ*, 135, 264
- Collin, S., Kawaguchi, T., Peterson, B. M., & Vestergaard, M. 2006, *A&A*, 456, 75
- Crenshaw, D. M., Kraemer, S. B., Bruhweiler, F. C., & Ruiz, J. R. 2001, *ApJ*, 555, 633
- Denney, K. D., Peterson, B. M., Dietrich, M., Vestergaard, M., & Bentz, M. C. 2009a, *ApJ*, 692, 246
- Denney, K. D., et al. 2006, *ApJ*, 653, 152
- . 2009b, *ApJ*, 702, 1353
- . 2009c, *ApJ*, 704, L80
- Di Matteo, T., Springel, V., & Hernquist, L. 2005, *Nature*, 433, 604
- Doroshenko, V. T., Sergeev, S. G., Merkulova, N. I., Sergeeva, E. A., Golubinsky, Y. V., Pronik, V. I., & Okhmat, N. N. 2005a, *Astrophysics*, 48, 156
- . 2005b, *Astrophysics*, 48, 304
- Edelson, R. A., & Krolik, J. H. 1988, *ApJ*, 333, 646
- Ferrarese, L., & Ford, H. 2005, *Space Science Reviews*, 116, 523

- Ferrarese, L., & Merritt, D. 2000, *ApJ*, 539, L9
- Ferrarese, L., Pogge, R. W., Peterson, B. M., Merritt, D., Wandel, A., & Joseph, C. L. 2001, *ApJ*, 555, L79
- Gaskell, C. M., Goosmann, R. W., Antonucci, R. R. J., & Whysong, D. H. 2004, *ApJ*, 616, 147
- Gaskell, C. M., & Peterson, B. M. 1987, *ApJS*, 65, 1
- Gaskell, C. M., & Sparke, L. S. 1986, *ApJ*, 305, 175
- Gebhardt, K., & Thomas, J. 2009, *ApJ*, 700, 1690
- Gebhardt, K., et al. 2000a, *ApJ*, 539, L13
- . 2000b, *ApJ*, 543, L5
- Graham, A. W. 2007, *MNRAS*, 379, 711
- Gültekin, K., Richstone, D. O., Gebhardt, K., Lauer, T. R., Tremaine, S., Aller, M. C., Bender, R., Dressler, A., Faber, S. M., Filippenko, A. V., Green, R., Ho, L. C., Kormendy, J., Magorrian, J., Pinkney, J., & Siopis, C. 2009, *ApJ*, 698, 198
- Häring, N., & Rix, H. 2004, *ApJ*, 604, L89
- Hopkins, P. F., & Hernquist, L. 2009, *ApJ*, 694, 599
- Horne, K., Peterson, B. M., Collier, S. J., & Netzer, H. 2004, *PASP*, 116, 465
- Kaspi, S., Brandt, W. N., Maoz, D., Netzer, H., Schneider, D. P., & Shemmer, O. 2007, *ApJ*, 659, 997
- Kaspi, S., Maoz, D., Netzer, H., Peterson, B. M., Vestergaard, M., & Jannuzi, B. T. 2005, *ApJ*, 629, 61
- Kaspi, S., Smith, P. S., Netzer, H., Maoz, D., Jannuzi, B. T., & Giveon, U. 2000, *ApJ*, 533, 631
- Klimek, E. S., Gaskell, C. M., & Hedrick, C. H. 2004, *ApJ*, 609, 69
- Kobayashi, Y., Yoshii, Y., & Minezaki, T. 2004, *Astronomische Nachrichten*, 325, 537
- Kobayashi, Y., Yoshii, Y., Peterson, B. A., Minezaki, T., Enya, K., Suganuma, M., & Yamamuro, T. 1998a, in *Proc. SPIE*, Vol. 3354, 769–776

- Kobayashi, Y., et al. 1998b, in Proc. SPIE, Vol. 3352, 120–128
- Kollmeier, J. A., et al. 2006, ApJ, 648, 128
- Korista, K. T., & Goad, M. R. 2004, ApJ, 606, 749
- Kormendy, J., & Gebhardt, K. 2001, in American Institute of Physics Conference Series, Vol. 586, 20th Texas Symposium on relativistic astrophysics, ed. J. C. Wheeler & H. Martel, 363–381
- Kormendy, J., & Richstone, D. 1995, ARA&A, 33, 581
- Magorrian, J., et al. 1998, AJ, 115, 2285
- Marconi, A., Axon, D. J., Maiolino, R., Nagao, T., Pastorini, G., Pietrini, P., Robinson, A., & Torricelli, G. 2008, ApJ, 678, 693
- Marconi, A., Axon, D. J., Maiolino, R., Nagao, T., Pietrini, P., Risaliti, G., Robinson, A., & Torricelli, G. 2009, ApJ, 698, L103
- McLure, R. J., & Dunlop, J. S. 2004, MNRAS, 352, 1390
- Minezaki, T., Yoshii, Y., Kobayashi, Y., Enya, K., Suganuma, M., Tomita, H., Aoki, T., & Peterson, B. A. 2004, ApJ, 600, L35
- Murray, N., Chiang, J., Grossman, S. A., & Voit, G. M. 1995, ApJ, 451, 498
- Nelson, C. H., Green, R. F., Bower, G., Gebhardt, K., & Weistrop, D. 2004, ApJ, 615, 652
- Netzer, H. 2009, ApJ, 695, 793
- Netzer, H., & Maoz, D. 1990, ApJ, 365, L5
- Onken, C. A., Ferrarese, L., Merritt, D., Peterson, B. M., Pogge, R. W., Vestergaard, M., & Wandel, A. 2004, ApJ, 615, 645
- Onken, C. A., Peterson, B. M., Dietrich, M., Robinson, A., & Salamanca, I. M. 2003, ApJ, 585, 121
- Peterson, B. M. 1993, PASP, 105, 247
- Peterson, B. M. 2001, in Advanced Lectures on the Starburst-AGN Connection, ed. I. Aretxaga, D. Kunth, & R. Mújica (Singapore: World Scientific), p. 3
- . 2010, in prep, (see also arXiv1001.3675)

- Peterson, B. M., Wanders, I., Bertram, R., Hunley, J. F., Pogge, R. W., & Wagner, R. M. 1998, *ApJ*, 501, 82
- Peterson, B. M., et al. 1991, *ApJ*, 368, 119
- . 2000, *ApJ*, 542, 161
- . 2002, *ApJ*, 581, 197
- . 2004, *ApJ*, 613, 682
- Salamanca, I., et al. 1994, *A&A*, 282, 742
- Salviander, S., Shields, G. A., Gebhardt, K., & Bonning, E. W. 2007, *ApJ*, 662, 131
- Schlegel, D. J., Finkbeiner, D. P., & Davis, M. 1998, *ApJ*, 500, 525
- Sergeev, S. G., Doroshenko, V. T., Dzyuba, S. A., Peterson, B. M., Pogge, R. W., & Pronik, V. I. 2007, *ApJ*, 668, 708
- Sergeev, S. G., Doroshenko, V. T., Golubinskiy, Y. V., Merkulova, N. I., & Sergeeva, E. A. 2005, *ApJ*, 622, 129
- Shankar, F., Weinberg, D. H., & Miralda-Escudé, J. 2009, *ApJ*, 690, 20
- Shen, J., & Gebhardt, K. 2010, *ApJ*, 711, 484
- Shen, Y., Greene, J. E., Strauss, M. A., Richards, G. T., & Schneider, D. P. 2008, *ApJ*, 680, 169
- Silk, J., & Rees, M. J. 1998, *A&A*, 331, L1
- Snedden, S. A., & Gaskell, C. M. 2007, *ApJ*, 669, 126
- Somerville, R. S., Hopkins, P. F., Cox, T. J., Robertson, B. E., & Hernquist, L. 2008, *MNRAS*, 391, 481
- Suganuma, M., et al. 2006, *ApJ*, 639, 46
- Tremaine, S., et al. 2002, *ApJ*, 574, 740
- van den Bosch, R. C. E., & de Zeeuw, P. T. 2010, *MNRAS*, 401, 1770
- van Groningen, E., & Wanders, I. 1992, *PASP*, 104, 700

- Vestergaard, M., Fan, X., Tremonti, C. A., Osmer, P. S., & Richards, G. T. 2008, *ApJ*, 674, L1
- Vestergaard, M., & Osmer, P. S. 2009, *ApJ*, 699, 800
- Wandel, A. 2002, *ApJ*, 565, 762
- Wandel, A., Peterson, B. M., & Malkan, M. A. 1999, *ApJ*, 526, 579
- Wanders, I., Peterson, B. M., Pogge, R. W., Derobertis, M. M., & van Groningen, E. 1992, *A&A*, 266, 72
- Wanders, I., et al. 1993, *A&A*, 269, 39
- Welsh, W. F. 1999, *PASP*, 111, 1347
- White, R. J., & Peterson, B. M. 1994, *PASP*, 106, 879
- Whittle, M. 1992, *ApJS*, 79, 49
- Winge, C., Peterson, B. M., Horne, K., Pogge, R. W., Pastoriza, M. G., & Storchi-Bergmann, T. 1995, *ApJ*, 445, 680
- Woo, J., et al. 2010, *ApJ*, 716, 269
- Yoshii, Y. 2002, in *New Trends in Theoretical and Observational Cosmology*, ed. K. Sato & T. Shiromizu (Tokyo: Universal Academy), 235

Table 1. Object List

Objects	z	α_{2000} (hr min sec)	δ_{2000} ($^{\circ}$ ' ")	Host Classification	A_B (mag)
(1)	(2)	(3)	(4)	(5)	(6)
Mrk 290	0.02958	15 35 52.3	+57 54 09	E1	0.065
Mrk 817	0.03145	14 36 22.1	+58 47 39	SBc	0.029
NGC 3227	0.00386	10 23 30.6	+19 51 54	SAB(s) pec	0.76 ^a
NGC 3516	0.00884	11 06 47.5	+72 34 07	(R)SB(s)	1.70 ^a
NGC 4051	0.00234	12 03 09.6	+44 31 53	SAB(rs)bc	0.056
NGC 5548	0.01717	14 17 59.5	+25 08 12	(R')SA(s)0/a	0.088

^aValues have been adjusted to account for additional internal reddening as described in section 5.2.

Table 2. Spectroscopic Observations

Objects (1)	Observ. (2)	N_{obs} (3)	Julian Dates (-2450000) (4)	Res (\AA) (5)	5100 \AA Cont. Window (\AA) (6)	H β Line Limits (\AA) (7)	Extraction Window ($''$) (8)
Mrk 290	MDM	71	4184–4268	7.6	5235–5265	4915–5086 ^{a,b}	5.0 \times 12.75
	CrAO	18	4266–4301	7.5	5235–5265	4915–5086	3.0 \times 11.0
	DAO	11	4262–4290	7.9	5235–5265	4915–5086	3.0 \times 6.28
Mrk 817	MDM	65	4185–4269	7.6	5245–5275	4900–5099	5.0 \times 12.75
	CrAO	23	4265–4301	7.5	5245–5275	4900–5099	3.0 \times 11.0
NGC 3227	MDM	75	4184–4268	7.6	5105–5135	4795–4942 ^{a,b}	5.0 \times 8.25
NGC 3516	MDM	74	4184–4269	7.6	5130–5160	4845–4965 ^b	5.0 \times 12.75
	CrAO	19	4266–4300	7.5	5130–5160	4845–4965 ^b	3.0 \times 11.0
NGC 4051	MDM	86	4184–4269	7.6	5090–5130	4815–4920	5.0 \times 12.75
	CrAO	22	4266–4300	7.5	5090–5130	4815–4920	3.0 \times 11.0
NGC 5548	MDM	77	4184–4267	7.6	5170–5200	4845–5004 ^b	5.0 \times 12.75
	CrAO	20	4265–4301	7.5	5170–5200	4845–5004 ^b	3.0 \times 11.0
	DAO	11	4276–4293	7.9	5170–5200	4845–5000 ^b	3.0 \times 6.28

^aH β line limits were narrowed for the measurement of the line width in the rms spectrum. See Section 3 for details.

^bH β line limits were changed for the velocity-resolved lag investigation. See Section 4 for details.

Table 3. Photometric Observations

Objects (1)	Observatory (2)	N_{obs} (3)	Julian Dates (-2450000) (4)
Mrk 290	MAGNUM	17	4200–4321
	CrAO	61	4180–4298
	UNebr	6	4199–4252
Mrk 817	MAGNUM	24	4185–4330
	CrAO	69	4180–4299
NGC 3227	MAGNUM	19	4181–4282
	CrAO	58	4180–4263
	UNebr	19	4195–4276
NGC 3516	MAGNUM	10	4190–4277
	CrAO	73	4181–4299
	UNebr	22	4195–4258
NGC 4051	MAGNUM	23	4182–4311
	CrAO	76	4180–4299
	UNebr	28	4195–4290
NGC 5548	MAGNUM	48	4182–4332
	CrAO	71	4180–4299
	UNebr	13	4198–4289

Table 4. Constant Spectral Properties

Objects (1)	FWHM([O III] λ 5007) ^a rest frame (km s ⁻¹) (2)	F ([O III] λ 5007) (10 ⁻¹³ ergs s ⁻¹ cm ⁻²) (3)	H β _{nar} Line Strength ^b (4)	F _{Host} (10 ⁻¹⁵ ergs s ⁻¹ cm ⁻² Å ⁻¹) (5)
Mrk 290	380	1.91 ± 0.12	0.08	1.79
Mrk 817	330	1.32 ± 0.07	0.08	1.84 ± 0.17
NGC 3227	485	6.81 ± 0.54	0.088 ^c	7.30 ± 0.67
NGC 3516	250	3.35 ± 0.42	0.07	16.1 ± 1.5
NGC 4051	190	3.91 ± 0.12 ^c	...	9.18 ± 0.85
NGC 5548	410	5.58 ± 0.27 ^d	0.11 ^e	4.48 ± 0.41

^aFrom Whittle (1992).

^bRatio of narrow F (H β _{nar}) to F ([O III] λ 5007).

^cFrom Peterson et al. (2000).

^dFrom Peterson et al. (1991).

^eFrom Peterson et al. (2004).

Table 5. *V*-band and Continuum Fluxes

Mrk 290		Mrk 817		NGC 3227		NGC 3516		NGC 5548	
JD ^a	$F_{\text{cont}}^{\text{b}}$								
4180.47p	1.083±0.015	4180.44p	4.621±0.038	4180.28p	3.959±0.064	4181.33p	6.433±0.104	4180.41p	2.800±0.055
4181.54p	1.070±0.015	4181.52p	4.622±0.036	4181.32p	3.971±0.057	4182.39p	6.135±0.126	4181.50p	2.878±0.058
4184.97m	1.102±0.047	4185.02g	4.654±0.048	4181.90g	3.250±0.052	4184.74m	5.574±0.364	4182.06g	3.128±0.032
4185.96m	1.109±0.047	4185.92m	4.602±0.078	4182.36p	3.836±0.059	4185.66m	5.897±0.369	4184.92m	2.912±0.118
4186.61p	1.102±0.033	4186.60p	4.744±0.060	4184.68m	3.363±0.149	4186.47p	5.753±0.162	4185.86m	2.643±0.114
4186.94m	1.194±0.048	4186.87m	4.552±0.077	4185.61m	3.623±0.153	4187.36p	5.823±0.139	4186.58p	2.709±0.062
4187.48p	1.184±0.021	4187.46p	4.834±0.052	4186.45p	3.857±0.058	4188.35p	5.579±0.185	4186.83m	2.624±0.113
4187.96m	1.242±0.049	4188.49p	4.778±0.046	4187.35p	3.915±0.079	4188.66m	6.065±0.373	4188.47p	2.627±0.060
4188.52p	1.194±0.018	4188.91m	4.561±0.077	4187.61m	3.502±0.151	4189.36p	5.607±0.134	4188.86m	2.852±0.117
4188.95m	1.188±0.048	4189.52p	4.830±0.055	4188.34p	4.044±0.076	4189.71m	6.641±0.379	4189.50p	2.608±0.068
4189.54p	1.201±0.023	4189.86m	4.602±0.078	4188.61m	4.003±0.159	4190.39p	5.620±0.113	4189.81m	2.556±0.113
4189.90m	1.229±0.049	4190.55p	4.720±0.082	4190.61m	3.994±0.158	4190.66m	5.847±0.371	4189.88g	2.569±0.038
4190.56p	1.167±0.025	4191.13g	4.835±0.136	4191.36p	3.961±0.104	4190.78g	5.424±0.108	4190.53p	2.676±0.081
4190.93m	1.274±0.050	4191.53p	4.746±0.072	4191.66m	4.012±0.159	4191.31p	5.722±0.137	4190.88m	2.413±0.111
4191.55p	1.225±0.033	4191.86m	4.796±0.080	4192.42p	4.053±0.096	4191.71m	5.205±0.359	4191.50p	2.487±0.112
4191.95m	1.205±0.048	4192.56p	4.756±0.059	4192.61m	4.495±0.165	4192.40p	5.691±0.179	4191.81m	2.771±0.116
4192.58p	1.187±0.026	4192.90m	4.734±0.079	4193.66m	4.096±0.160	4192.66m	4.738±0.351	4191.86g	2.437±0.036
4192.94m	1.270±0.050	4194.92m	4.772±0.080	4193.80g	3.737±0.031	4193.75m	4.686±0.351	4192.54p	2.414±0.125
4194.96m	1.249±0.049	4200.55p	4.786±0.042	4194.62m	3.892±0.157	4194.68m	4.744±0.352	4192.85m	2.660±0.114
4197.97m	1.149±0.047	4201.12g	4.822±0.222	4195.37n	4.332±0.053	4195.43n	5.188±0.160	4193.71m	2.778±0.116
4199.40n	1.181±0.043	4201.43p	4.776±0.052	4195.69m	4.430±0.164	4196.67m	4.784±0.352	4194.10g	2.203±0.078
4199.98m	1.219±0.049	4201.90m	4.803±0.080	4196.38p	3.843±0.225	4197.70m	5.188±0.355	4194.87m	2.582±0.113
4200.36g	1.185±0.026	4202.52p	4.821±0.049	4196.81m	3.910±0.157	4198.44n	5.196±0.150	4197.81g	2.355±0.051
4200.57p	1.128±0.016	4204.51p	4.958±0.110	4197.64m	3.836±0.156	4198.69m	5.952±0.373	4197.92m	2.417±0.111
4201.46p	1.140±0.017	4204.85m	4.791±0.080	4197.96g	3.897±0.036	4198.90g	5.927±0.083	4198.60n	2.491±0.130
4201.95m	1.217±0.049	4205.46p	4.936±0.039	4198.40n	3.911±0.072	4199.34p	5.886±0.096	4198.84m	2.338±0.109
4202.54p	1.153±0.019	4205.86m	5.002±0.082	4198.64m	4.087±0.160	4199.40n	5.751±0.110	4199.06g	2.353±0.043
4204.50p	1.110±0.017	4206.50p	4.874±0.058	4199.32p	4.201±0.057	4200.37p	5.766±0.125	4199.51p	2.337±0.068
4204.90m	1.063±0.046	4207.11g	5.174±0.214	4199.39n	4.151±0.072	4200.67m	5.386±0.362	4199.93m	2.326±0.109
4205.49p	1.090±0.019	4207.92m	5.046±0.082	4199.63m	4.235±0.161	4201.29p	5.964±0.134	4200.53p	2.367±0.056
4205.96m	1.059±0.046	4208.48p	5.043±0.053	4200.36p	4.278±0.059	4201.67m	6.523±0.382	4200.83m	2.461±0.111
4206.40n	1.071±0.064	4208.88m	4.983±0.081	4200.62m	4.597±0.166	4202.35p	5.754±0.121	4201.05g	2.368±0.029
4207.97m	1.013±0.045	4209.53p	5.164±0.048	4200.84g	4.483±0.045	4204.69m	5.953±0.372	4201.41p	2.341±0.055
4208.44p	1.043±0.015	4209.89m	5.050±0.082	4201.28p	4.451±0.071	4205.31p	6.019±0.138	4201.85m	2.303±0.108
4208.92m	0.978±0.044	4210.89m	5.012±0.082	4201.62m	4.606±0.167	4205.71m	6.267±0.374	4202.49p	2.370±0.055
4209.55p	1.024±0.017	4212.51p	5.130±0.045	4202.34p	4.482±0.061	4205.90g	5.780±0.239	4203.02g	2.363±0.029
4209.94m	0.975±0.044	4212.88m	5.108±0.083	4203.84g	4.433±0.025	4206.34p	5.895±0.138	4204.47p	2.418±0.065
4210.96m	1.030±0.045	4213.48p	5.177±0.039	4204.31p	4.489±0.057	4206.40n	5.780±0.181	4204.79m	2.362±0.109
4212.52p	1.064±0.024	4213.89m	5.110±0.083	4204.64m	4.402±0.164	4206.73m	5.645±0.363	4205.54p	2.237±0.052
4212.58g	1.085±0.007	4214.48p	5.208±0.050	4205.27p	4.381±0.055	4207.40n	6.215±0.140	4205.82m	2.255±0.108
4212.95m	1.065±0.046	4214.88m	5.178±0.084	4205.67m	4.532±0.166	4208.39p	6.112±0.155	4206.45p	2.305±0.051
4213.50p	1.037±0.015	4215.89m	5.231±0.085	4206.32p	4.265±0.062	4208.40n	6.277±0.181	4206.60n	2.064±0.156
4213.96m	1.041±0.045	4216.49p	5.147±0.042	4206.39n	4.271±0.086	4208.72m	5.656±0.369	4206.82m	2.212±0.107
4214.43p	1.070±0.017	4216.88m	5.210±0.084	4206.67m	4.198±0.161	4209.38p	6.189±0.127	4207.87m	2.279±0.108

Table 5—Continued

Mrk 290		Mrk 817		NGC 3227		NGC 3516		NGC 5548	
JD ^a	$F_{\text{cont}}^{\text{b}}$								
4214.95m	1.078±0.046	4217.48p	5.059±0.066	4207.39m	4.128±0.072	4209.73m	5.659±0.367	4208.37p	2.437±0.053
4215.96m	1.034±0.045	4217.89m	5.013±0.082	4207.77m	4.346±0.163	4210.40n	6.825±0.150	4208.83m	2.219±0.107
4216.54p	1.076±0.014	4218.51p	5.172±0.043	4207.82g	4.009±0.056	4210.72m	6.637±0.385	4208.99g	2.114±0.069
4216.95m	1.098±0.046	4218.90m	5.106±0.083	4208.32p	4.301±0.059	4211.38p	5.942±0.098	4209.50p	2.259±0.051
4217.50p	1.108±0.018	4219.03g	5.208±0.026	4208.36n	4.203±0.119	4212.32p	5.904±0.096	4209.84m	2.160±0.107
4217.93m	1.102±0.047	4219.52p	5.280±0.047	4208.67m	4.077±0.160	4212.67m	6.556±0.383	4210.08g	2.208±0.049
4218.53p	1.112±0.017	4220.45p	5.117±0.059	4209.37p	4.204±0.058	4213.28p	5.921±0.111	4210.84m	2.214±0.107
4218.95m	1.094±0.046	4220.91m	5.079±0.083	4209.65m	4.114±0.160	4213.69m	5.446±0.365	4211.53p	2.284±0.060
4220.40n	1.067±0.043	4221.48p	5.192±0.073	4210.30n	4.332±0.072	4213.77g	6.283±0.114	4212.83m	2.203±0.107
4220.48p	1.084±0.024	4222.90m	5.200±0.084	4210.67m	4.291±0.162	4214.31p	5.884±0.128	4212.89g	2.257±0.035
4220.96m	1.139±0.047	4223.50p	5.316±0.065	4210.90g	4.044±0.091	4214.68m	5.957±0.371	4213.45p	2.238±0.053
4221.57g	1.073±0.050	4223.90m	5.421±0.087	4211.34p	4.150±0.055	4215.69m	5.740±0.368	4213.85m	2.075±0.105
4221.98m	1.131±0.047	4224.48p	5.407±0.071	4212.30p	3.963±0.055	4216.31p	5.694±0.129	4214.40p	2.250±0.056
4222.53p	1.067±0.025	4224.90m	5.287±0.085	4212.62m	3.892±0.157	4216.68m	6.342±0.377	4214.84m	2.121±0.105
4222.95m	1.137±0.047	4225.49p	5.408±0.058	4213.33p	3.924±0.059	4217.37p	6.017±0.137	4215.45p	2.155±0.095
4223.53p	1.098±0.024	4226.06g	5.511±0.081	4214.29p	3.868±0.067	4217.68m	5.616±0.368	4215.85m	2.081±0.105
4223.94m	1.119±0.047	4226.44p	5.447±0.064	4214.63m	3.920±0.157	4218.44p	5.687±0.107	4216.46p	2.089±0.057
4224.45p	1.094±0.024	4226.89m	5.569±0.089	4215.37p	4.130±0.066	4218.75m	4.792±0.353	4216.84m	2.020±0.104
4224.94m	1.195±0.048	4227.53p	5.447±0.085	4215.64m	4.049±0.159	4219.28p	5.851±0.110	4217.44p	2.041±0.061
4225.52p	1.035±0.026	4227.90m	5.542±0.089	4216.63m	3.901±0.157	4219.40n	6.157±0.201	4217.84m	2.115±0.105
4225.92m	1.134±0.047	4228.91m	5.718±0.091	4217.31p	4.427±0.071	4219.79m	5.235±0.360	4218.47p	1.984±0.060
4226.42p	1.055±0.019	4229.53p	5.500±0.066	4217.63m	4.866±0.171	4220.27p	5.506±0.130	4218.77g	2.045±0.069
4226.94m	1.020±0.045	4229.88m	5.545±0.089	4218.29p	4.269±0.058	4220.40n	5.919±0.160	4218.86m	2.066±0.105
4227.95m	0.988±0.044	4230.91m	5.524±0.088	4218.30n	4.417±0.086	4220.69m	5.547±0.367	4219.50p	1.830±0.066
4228.94m	0.965±0.044	4231.45p	5.385±0.063	4218.70m	4.337±0.163	4221.33p	6.051±0.199	4219.88m	2.136±0.105
4229.45p	0.953±0.014	4231.91m	5.317±0.086	4219.30p	4.419±0.106	4221.69m	5.436±0.365	4220.41p	2.017±0.095
4229.93m	0.941±0.043	4232.02g	5.494±0.210	4219.30n	4.239±0.068	4221.84g	6.462±0.146	4220.60n	1.968±0.143
4230.95m	0.896±0.043	4232.43p	5.275±0.039	4219.74m	4.606±0.167	4222.38p	5.601±0.149	4220.86m	1.885±0.101
4231.43p	0.927±0.017	4232.90m	5.449±0.087	4219.93g	4.066±0.051	4222.69m	5.916±0.371	4221.07g	2.063±0.034
4231.50g	0.880±0.035	4233.44p	5.275±0.052	4220.29p	4.232±0.075	4223.34p	5.867±0.168	4221.46p	1.997±0.090
4231.95m	0.882±0.043	4233.89m	5.407±0.087	4220.31n	4.500±0.099	4223.69m	5.786±0.371	4221.84m	2.055±0.104
4232.38p	0.860±0.014	4234.43p	5.215±0.040	4220.64m	4.411±0.164	4224.35p	5.725±0.149	4222.51p	1.890±0.095
4232.94m	0.832±0.042	4234.89m	5.316±0.086	4221.32p	4.320±0.080	4224.69m	5.706±0.370	4222.85m	2.042±0.104
4233.47p	0.863±0.014	4235.44p	5.270±0.046	4221.35n	4.351±0.073	4226.39p	5.709±0.155	4223.05g	1.942±0.094
4233.94m	0.816±0.042	4235.90m	5.358±0.086	4221.64m	4.254±0.161	4226.71m	5.376±0.362	4223.48p	2.029±0.073
4234.46p	0.824±0.014	4236.45p	5.199±0.045	4222.37p	4.345±0.073	4227.41p	5.486±0.134	4223.85m	1.877±0.101
4234.94m	0.904±0.043	4236.90m	5.345±0.086	4222.63m	4.532±0.166	4227.69m	5.385±0.364	4224.41p	2.033±0.064
4235.46p	0.843±0.013	4237.44p	5.154±0.055	4223.36p	4.358±0.068	4229.42p	5.783±0.150	4224.85m	2.062±0.105
4235.94m	0.818±0.042	4237.90m	5.451±0.087	4223.64m	4.439±0.164	4229.73m	5.490±0.363	4225.06g	1.971±0.034
4236.95m	0.851±0.043	4239.90m	5.491±0.088	4223.83g	4.410±0.055	4230.27p	5.382±0.125	4225.46p	2.000±0.111
4237.42p	0.823±0.013	4239.93g	5.346±0.040	4224.33p	4.365±0.061	4230.69m	5.340±0.362	4225.89m	1.908±0.103
4237.95m	0.784±0.042	4240.48p	5.342±0.050	4224.63m	4.476±0.165	4231.41p	5.622±0.131	4226.37p	2.049±0.057
4238.49g	0.844±0.015	4240.89m	5.226±0.085	4225.33p	4.396±0.064	4231.70m	6.147±0.374	4226.83m	1.943±0.103
4239.57n	0.804±0.043	4241.44p	5.240±0.041	4226.26p	4.346±0.071	4232.35p	5.773±0.115	4227.50p	1.859±0.116
4239.94m	0.818±0.042	4241.89m	5.309±0.086	4226.64m	4.346±0.163	4232.68m	5.780±0.370	4227.86m	2.054±0.104

Table 5—Continued

Mrk 290		Mrk 817		NGC 3227		NGC 3516		NGC 5548	
JD ^a	$F_{\text{cont}}^{\text{b}}$								
4240.44p	0.873±0.024	4242.49p	5.213±0.050	4226.81g	4.447±0.045	4233.42n	5.834±0.231	4228.86m	1.932±0.103
4240.93m	0.858±0.043	4243.51p	5.262±0.051	4227.64m	4.207±0.161	4233.68m	6.766±0.382	4229.40p	2.046±0.049
4241.47p	0.864±0.015	4243.90m	5.303±0.086	4228.75m	4.653±0.167	4234.30p	5.854±0.120	4229.84m	2.078±0.105
4241.93m	0.876±0.043	4244.90m	5.202±0.084	4229.34p	4.257±0.061	4234.68m	6.876±0.388	4230.86m	1.954±0.103
4242.45p	0.871±0.018	4245.45p	5.194±0.041	4229.68m	4.384±0.163	4235.29p	5.756±0.118	4231.38p	1.977±0.052
4242.94m	0.899±0.043	4245.90m	5.220±0.085	4230.64m	4.560±0.166	4235.44n	6.320±0.301	4231.84g	1.873±0.079
4243.46p	0.922±0.014	4246.51p	5.196±0.044	4231.32p	4.375±0.057	4235.68m	6.184±0.377	4231.86m	1.887±0.101
4243.95m	0.966±0.044	4246.89m	5.096±0.083	4231.65m	4.346±0.163	4236.27p	6.186±0.118	4232.33p	2.058±0.047
4244.94m	0.944±0.044	4247.84g	5.206±0.020	4232.27p	4.303±0.058	4236.68m	6.785±0.386	4232.85m	1.985±0.104
4245.48p	0.934±0.016	4247.88m	5.158±0.084	4232.63m	4.272±0.162	4237.38p	5.884±0.101	4233.43p	2.024±0.048
4245.95m	0.889±0.043	4248.89m	5.120±0.083	4233.30p	4.390±0.057	4237.50n	6.235±0.251	4233.85m	2.002±0.104
4246.49p	0.915±0.014	4249.51p	5.127±0.047	4233.38n	4.650±0.133	4237.69m	6.212±0.378	4234.41p	1.902±0.048
4246.50n	0.994±0.043	4249.89m	5.028±0.082	4233.63m	4.727±0.168	4238.46n	5.375±0.271	4234.85m	2.067±0.105
4246.94m	0.889±0.043	4250.89m	5.049±0.082	4234.29p	4.474±0.058	4238.68m	5.997±0.373	4234.93g	2.041±0.027
4247.93m	0.918±0.043	4251.48p	5.135±0.064	4234.64m	4.523±0.165	4239.48p	5.676±0.154	4235.41p	1.997±0.049
4248.94m	0.914±0.043	4251.89m	4.822±0.080	4234.81g	4.764±0.035	4239.70m	5.400±0.363	4235.85m	2.003±0.104
4249.53p	0.875±0.019	4252.54p	5.036±0.111	4235.27p	4.543±0.057	4240.33p	5.426±0.119	4236.41p	2.115±0.047
4250.94m	0.829±0.042	4252.88m	5.082±0.083	4235.46n	4.874±0.113	4240.52n	5.741±0.261	4236.85m	2.020±0.104
4251.44p	0.791±0.026	4253.01g	5.119±0.058	4235.64m	4.476±0.165	4240.68m	6.180±0.376	4237.35p	1.955±0.047
4252.49g	0.770±0.015	4253.89m	4.987±0.082	4236.29p	4.520±0.055	4241.27p	5.557±0.120	4237.60n	1.960±0.195
4252.49p	0.763±0.022	4254.85m	4.924±0.081	4236.63m	4.569±0.166	4241.45n	5.615±0.281	4237.85m	1.942±0.103
4252.57n	0.716±0.085	4255.48p	4.958±0.057	4237.26p	4.501±0.058	4241.68m	6.231±0.377	4237.92g	2.047±0.027
4252.93m	0.795±0.042	4255.86m	4.780±0.080	4237.64m	4.467±0.165	4242.35p	5.518±0.106	4238.57n	2.167±0.182
4253.94m	0.764±0.041	4256.50p	5.061±0.052	4238.63m	4.467±0.165	4242.40n	5.558±0.311	4239.45p	2.062±0.057
4254.90m	0.734±0.041	4256.87m	4.868±0.080	4238.79g	4.764±0.024	4242.70m	5.973±0.372	4239.85m	1.990±0.104
4255.51p	0.723±0.020	4257.49p	4.951±0.044	4239.30p	4.374±0.061	4243.35p	5.110±0.136	4239.96g	2.041±0.027
4255.91m	0.584±0.038	4258.51p	5.007±0.062	4239.33n	4.204±0.120	4243.69m	5.861±0.371	4240.40p	2.032±0.053
4256.47p	0.715±0.017	4258.88m	5.094±0.083	4239.66m	4.616±0.167	4244.75m	5.083±0.357	4240.84m	1.912±0.103
4256.91m	0.628±0.039	4259.42p	4.951±0.039	4240.31p	4.542±0.059	4245.30p	4.978±0.136	4241.38p	2.016±0.068
4257.46p	0.725±0.015	4259.89m	5.012±0.082	4240.63m	4.783±0.169	4245.69m	4.521±0.349	4241.50n	2.176±0.195
4257.94m	0.610±0.038	4259.99g	4.935±0.094	4241.29p	4.641±0.058	4246.36n	4.467±0.171	4241.84m	2.236±0.108
4258.48p	0.724±0.015	4260.49p	4.959±0.043	4241.63m	4.912±0.171	4246.37p	5.193±0.117	4241.97g	2.043±0.053
4258.93m	0.665±0.039	4260.89m	4.788±0.080	4242.33p	4.903±0.061	4246.69m	4.262±0.343	4242.38p	2.078±0.049
4259.45p	0.696±0.014	4261.41p	4.924±0.038	4242.64m	4.829±0.170	4247.69m	4.152±0.342	4242.92m	1.960±0.103
4259.47g	0.636±0.014	4261.89m	4.820±0.080	4243.31p	4.726±0.069	4247.86g	5.191±0.127	4243.38p	2.063±0.049
4259.94m	0.689±0.040	4262.42p	4.952±0.038	4243.64m	5.024±0.173	4248.36p	4.939±0.134	4243.85m	1.971±0.103
4260.44p	0.689±0.012	4263.44p	4.978±0.041	4244.68m	5.191±0.174	4248.69m	4.731±0.353	4244.85m	2.033±0.104
4260.94m	0.612±0.038	4263.86m	4.840±0.080	4245.33p	4.901±0.122	4249.30p	4.879±0.129	4245.43p	2.076±0.065
4261.44p	0.665±0.012	4264.86m	5.005±0.082	4245.65m	5.126±0.174	4249.69m	5.083±0.359	4245.85m	2.133±0.105
4261.93m	0.594±0.038	4264.92g	4.875±0.037	4246.34n	4.992±0.080	4250.28p	5.302±0.199	4245.89g	2.007±0.066
4262.45p	0.625±0.014	4265.44c	4.870±0.094	4246.64m	5.033±0.173	4250.69m	4.822±0.354	4246.40p	2.172±0.057
4262.45g	0.667±0.014	4265.88m	4.967±0.081	4246.76g	4.919±0.057	4251.34p	5.179±0.156	4246.85m	2.023±0.104
4262.84d	0.603±0.057	4266.44c	5.125±0.097	4247.65m	4.820±0.170	4251.69m	4.258±0.345	4247.84m	2.042±0.104
4263.50p	0.679±0.014	4266.86m	5.041±0.082	4248.30p	4.608±0.084	4252.37p	4.897±0.145	4248.41p	2.194±0.164
4263.91m	0.636±0.039	4267.42c	4.985±0.095	4248.64m	4.718±0.168	4252.49n	4.360±0.160	4248.85m	2.140±0.105

Table 5—Continued

Mrk 290		Mrk 817		NGC 3227		NGC 3516		NGC 5548	
JD ^a	$F_{\text{cont}}^{\text{b}}$								
4264.92m	0.645±0.039	4267.86m	4.985±0.082	4249.32p	4.522±0.086	4252.69m	4.536±0.347	4249.48p	1.985±0.074
4265.93m	0.681±0.040	4268.48c	5.206±0.098	4249.64m	4.643±0.167	4253.68m	5.022±0.353	4249.85m	2.241±0.108
4266.48c	0.728±0.057	4268.85m	4.899±0.080	4249.80g	4.749±0.066	4253.81g	5.044±0.064	4249.94g	2.153±0.034
4266.91m	0.703±0.040	4269.85m	4.852±0.080	4250.31p	4.513±0.122	4254.42n	4.558±0.211	4250.84m	2.188±0.107
4267.44c	0.704±0.056	4269.88g	4.922±0.025	4250.64m	4.374±0.163	4255.43p	4.199±0.120	4251.38p	2.212±0.079
4267.91d	0.771±0.041	4270.47c	4.909±0.095	4251.64m	4.254±0.161	4255.51n	4.368±0.291	4251.84m	2.110±0.105
4267.91m	0.713±0.060	4271.42c	4.800±0.093	4252.34p	4.219±0.072	4255.71m	4.081±0.341	4252.43p	2.116±0.088
4268.90m	0.762±0.041	4272.45c	4.846±0.094	4252.40n	4.214±0.067	4256.33p	4.295±0.116	4252.51n	1.967±0.156
4269.46c	0.755±0.058	4272.93g	4.849±0.055	4252.64m	4.096±0.160	4256.44n	4.633±0.251	4252.84m	2.258±0.108
4269.87d	0.798±0.062	4273.42c	4.956±0.095	4253.65m	3.873±0.157	4257.37p	4.542±0.087	4252.96g	2.221±0.048
4270.85d	0.841±0.063	4274.48c	4.870±0.094	4254.40n	3.844±0.080	4257.69m	3.544±0.333	4253.84m	2.077±0.105
4273.45c	0.996±0.063	4275.93g	4.900±0.031	4254.76g	4.596±0.050	4258.29p	4.365±0.143	4254.81m	2.093±0.105
4274.44c	0.946±0.062	4276.40c	4.941±0.095	4255.32p	4.603±0.058	4258.40n	4.378±0.181	4254.96g	2.249±0.042
4274.47g	0.847±0.020	4277.39c	4.902±0.095	4255.67m	4.402±0.164	4258.71m	4.111±0.341	4255.41p	2.215±0.062
4276.43g	0.863±0.012	4278.41p	4.891±0.056	4256.30p	4.598±0.058	4259.32p	4.073±0.099	4255.53n	2.159±0.182
4277.43c	0.936±0.062	4278.42c	4.919±0.095	4256.66m	4.179±0.161	4259.70m	4.091±0.336	4255.82m	2.305±0.109
4277.89d	0.891±0.064	4278.87g	4.809±0.037	4257.64m	3.994±0.158	4260.33p	4.104±0.098	4256.39p	2.388±0.056
4278.45p	0.880±0.018	4280.45p	4.734±0.097	4258.31p	4.362±0.084	4260.71m	3.871±0.334	4256.41n	2.392±0.130
4278.46c	0.879±0.061	4281.43p	4.802±0.059	4259.30p	4.203±0.054	4261.28p	4.108±0.121	4256.82m	2.492±0.112
4281.47p	0.912±0.024	4281.48c	4.510±0.089	4259.65m	3.650±0.153	4261.69m	3.127±0.323	4257.32p	2.427±0.047
4282.37g	0.892±0.014	4282.39p	4.738±0.054	4259.76g	3.848±0.111	4262.33p	3.566±0.116	4257.81m	2.654±0.114
4282.42p	0.885±0.027	4282.50c	4.535±0.089	4260.31p	4.116±0.060	4262.69m	3.147±0.321	4258.39n	2.389±0.182
4282.46c	0.881±0.061	4282.94g	4.596±0.053	4260.66m	4.152±0.161	4263.33p	3.638±0.098	4258.44p	2.431±0.056
4282.81d	0.996±0.067	4283.39c	4.694±0.092	4261.65m	3.836±0.156	4263.68m	3.264±0.323	4258.83m	2.557±0.113
4283.42c	0.848±0.060	4283.44p	4.701±0.041	4262.28p	3.965±0.061	4264.70m	2.746±0.319	4259.40p	2.459±0.052
4283.47p	0.941±0.026	4284.38c	4.582±0.090	4262.65m	3.613±0.153	4265.72m	1.946±0.301	4259.84m	2.523±0.112
4284.41c	0.837±0.060	4284.40p	4.788±0.044	4263.30p	4.018±0.056	4266.36c	2.037±0.345	4259.88g	2.550±0.021
4284.42p	0.895±0.024	4285.92g	4.574±0.100	4263.37n	3.963±0.060	4266.69m	2.377±0.310	4260.36p	2.550±0.049
4285.86d	0.816±0.062	4290.41c	4.925±0.095	4263.76g	3.831±0.089	4267.69m	1.946±0.303	4260.84m	2.363±0.109
4286.86d	0.822±0.062	4291.38c	4.805±0.093	4264.65m	3.752±0.155	4268.34c	1.732±0.339	4261.39p	2.543±0.049
4287.86d	0.835±0.063	4293.39p	5.078±0.038	4265.67m	4.161±0.161	4268.69m	1.604±0.296	4261.53n	2.866±0.195
4288.44g	0.807±0.015	4294.42p	5.005±0.046	4266.65m	4.430±0.164	4269.29c	2.226±0.348	4261.84m	2.774±0.116
4288.86d	0.686±0.060	4295.40p	5.046±0.057	4267.64m	4.968±0.172	4269.69m	1.165±0.288	4261.93g	2.488±0.056
4289.42c	0.870±0.061	4296.41p	5.089±0.041	4268.64m	4.950±0.172	4271.37c	1.918±0.342	4262.40p	2.430±0.095
4290.44c	0.813±0.059	4297.43c	5.190±0.098	4268.78g	4.645±0.105	4271.79g	1.964±0.297	4262.80m	2.495±0.112
4290.85d	0.800±0.062	4298.34p	5.194±0.034	4270.35n	4.901±0.100	4272.37c	1.700±0.338	4263.41p	2.418±0.051
4291.41c	0.826±0.059	4298.45c	5.219±0.099	4273.77g	4.896±0.048	4273.36c	1.744±0.339	4263.81m	2.609±0.113
4293.43p	0.826±0.014	4299.38c	5.070±0.096			4274.33c	2.763±0.358	4263.94g	2.462±0.042
4296.42c	0.846±0.060	4299.46p	5.218±0.074			4274.80g	2.895±0.084	4264.82m	2.284±0.108
4296.43p	0.860±0.017	4300.36c	5.175±0.098			4277.33c	3.374±0.370	4265.81m	2.333±0.109
4297.48c	0.983±0.063	4300.85g	5.266±0.059			4277.77g	2.843±0.141	4266.82m	2.177±0.107
4298.42c	1.034±0.064	4301.43c	5.217±0.099			4278.32c	3.672±0.376	4267.81m	2.169±0.107
4298.43p	0.905±0.016	4305.84g	5.270±0.117			4279.29c	3.371±0.370	4268.86g	2.199±0.040
4300.38g	0.920±0.033	4311.83g	5.655±0.027			4279.29p	3.253±0.187	4270.43n	2.309±0.182
4300.40c	0.994±0.063	4314.83g	5.656±0.041			4280.29c	2.974±0.362	4270.90g	2.332±0.021

Table 5—Continued

Mrk 290		Mrk 817		NGC 3227	NGC 3516		NGC 5548	
JD ^a	$F_{\text{cont}}^{\text{b}}$	JD ^a	$F_{\text{cont}}^{\text{b}}$	JD ^a $F_{\text{cont}}^{\text{b}}$	JD ^a	$F_{\text{cont}}^{\text{b}}$	JD ^a	$F_{\text{cont}}^{\text{b}}$
4301.46c	1.021±0.064	4319.83g	5.416±0.053		4280.41p	3.117±0.199	4272.89g	2.307±0.027
4306.36g	0.975±0.046	4330.77g	5.578±0.048		4281.30p	2.860±0.132	4274.87g	2.335±0.021
4310.33g	1.049±0.022				4281.42c	2.761±0.358	4276.84d	2.089±0.118
4318.33g	1.126±0.015				4282.31p	2.816±0.130	4276.87g	2.379±0.027
4321.33g	1.079±0.013				4283.29c	2.665±0.356	4277.80d	2.276±0.122
					4283.31p	3.087±0.112	4278.35p	2.318±0.104
					4284.29p	2.822±0.109	4278.83d	2.596±0.127
					4284.33c	2.548±0.354	4279.36p	2.348±0.082
					4290.28c	2.676±0.357	4281.37p	2.207±0.111
					4291.32c	2.386±0.351	4282.37p	2.337±0.086
					4293.29p	3.044±0.099	4282.76d	2.592±0.127
					4294.34p	2.712±0.092	4282.85g	2.474±0.027
					4295.35p	2.708±0.099	4283.41p	2.276±0.084
					4296.29p	2.561±0.102	4284.33p	2.221±0.066
					4296.31c	2.512±0.354	4284.90g	2.419±0.027
					4298.31p	2.797±0.087	4285.77d	2.311±0.122
					4299.33c	2.761±0.358	4286.76d	2.238±0.121
					4299.34p	2.986±0.097	4287.76d	2.341±0.122
					4300.30c	3.347±0.369	4288.76d	2.387±0.123
							4288.85g	2.541±0.021
							4289.39n	2.363±0.117
							4290.75d	2.716±0.130
							4290.85g	2.662±0.035
							4292.84d	2.617±0.127
							4293.36p	2.588±0.056
							4293.77d	2.686±0.129
							4294.82g	2.758±0.036
							4296.38p	2.539±0.056
							4298.38p	2.513±0.058
							4299.38p	2.652±0.053
							4299.83g	2.666±0.035
							4304.81g	2.940±0.051
							4307.84g	3.094±0.068
							4309.80g	3.012±0.036
							4311.81g	2.940±0.036
							4313.81g	2.726±0.070
							4318.81g	2.684±0.042
							4319.81g	2.515±0.048
							4320.80g	2.554±0.042
							4330.75g	2.414±0.034
							4332.77g	2.348±0.060

^aJulian Dates are -2450000 and include the following observatory code to indicate the origin of the observation: MDM — m, MAGNUM — g, CrAO spectroscopy — c, CrAO photometry — p, UNebr. — n, and DAO — d.

^bContinuum fluxes are in units of 10^{-15} ergs s^{-1} cm^{-2} \AA^{-1} and represent the average continuum flux density measured ~ 5100 \AA , rest-frame, from spectroscopic observations or the photometric V -band flux. Spectroscopic and photometric fluxes were scaled to a uniform scale as described in Section 2.3. All fluxes

have been corrected for host starlight contamination.

Table 6. $H\beta$ Fluxes

Mrk 290		Mrk 817		NGC 3227		NGC 3516		NGC 5548	
JD ^a	$F_{H\beta}$ ^b								
4184.97m	2.203±0.049	4185.92m	2.491±0.082	4184.68m	3.559±0.103	4184.74m	5.833±0.185	4184.92m	2.285±0.212
4185.96m	2.253±0.050	4186.87m	2.515±0.083	4185.61m	3.576±0.104	4185.66m	6.170±0.195	4185.86m	2.298±0.213
4186.94m	2.230±0.049	4188.91m	2.340±0.077	4187.61m	3.506±0.102	4188.66m	6.150±0.195	4186.83m	2.227±0.207
4187.96m	2.196±0.048	4189.86m	2.169±0.071	4188.61m	4.066±0.118	4189.71m	6.130±0.193	4188.86m	2.184±0.203
4188.95m	2.183±0.048	4191.86m	2.518±0.083	4190.61m	3.690±0.107	4190.66m	5.782±0.184	4189.81m	1.941±0.181
4189.90m	2.158±0.047	4192.90m	2.450±0.080	4191.66m	3.853±0.111	4191.71m	5.633±0.179	4190.88m	1.830±0.170
4190.93m	2.251±0.050	4194.92m	2.261±0.075	4192.61m	3.774±0.110	4192.66m	5.495±0.175	4191.81m	1.730±0.161
4191.95m	2.285±0.051	4201.90m	2.416±0.080	4193.66m	3.945±0.114	4193.75m	5.534±0.176	4192.85m	1.517±0.142
4192.94m	2.217±0.049	4204.85m	2.389±0.079	4194.62m	4.015±0.116	4194.68m	5.674±0.181	4193.71m	1.572±0.146
4194.96m	2.221±0.049	4205.86m	2.537±0.083	4195.69m	3.840±0.111	4196.67m	5.466±0.174	4194.87m	1.764±0.164
4197.97m	2.261±0.050	4207.92m	2.351±0.078	4196.81m	4.010±0.116	4197.70m	5.664±0.178	4197.92m	1.659±0.155
4199.98m	2.323±0.051	4208.88m	2.390±0.079	4197.64m	4.052±0.118	4198.69m	6.280±0.200	4198.84m	1.353±0.126
4201.95m	2.315±0.051	4209.89m	2.380±0.079	4198.64m	4.319±0.125	4200.67m	5.621±0.179	4199.93m	1.672±0.156
4204.90m	2.233±0.049	4210.89m	2.312±0.077	4199.63m	3.940±0.114	4201.67m	5.840±0.186	4200.83m	1.730±0.161
4205.96m	2.274±0.050	4212.88m	2.314±0.077	4200.62m	4.138±0.120	4204.69m	5.804±0.185	4201.85m	1.587±0.148
4207.97m	2.240±0.049	4213.89m	2.535±0.083	4201.62m	4.138±0.120	4205.71m	5.899±0.186	4204.79m	1.513±0.140
4208.92m	2.281±0.050	4214.88m	2.436±0.080	4204.64m	4.481±0.130	4206.73m	5.455±0.172	4205.82m	1.427±0.133
4209.94m	2.198±0.048	4215.89m	2.531±0.083	4205.67m	4.416±0.128	4208.72m	5.886±0.188	4206.82m	1.392±0.130
4210.96m	2.169±0.048	4216.88m	2.367±0.078	4206.67m	4.539±0.132	4209.73m	6.035±0.192	4207.87m	1.456±0.135
4212.95m	2.169±0.048	4217.89m	2.293±0.076	4207.77m	4.573±0.133	4210.72m	6.305±0.201	4208.83m	1.581±0.147
4213.96m	2.220±0.049	4218.90m	2.536±0.083	4208.67m	4.636±0.135	4212.67m	6.385±0.204	4209.84m	1.522±0.142
4214.95m	2.214±0.049	4220.91m	2.538±0.083	4209.65m	4.672±0.135	4213.69m	5.732±0.183	4210.84m	1.629±0.152
4215.96m	2.214±0.049	4222.90m	2.375±0.079	4210.67m	4.708±0.136	4214.68m	6.438±0.204	4212.83m	1.414±0.131
4216.95m	2.129±0.047	4223.90m	2.486±0.082	4212.62m	4.658±0.135	4215.69m	5.980±0.190	4213.85m	1.297±0.121
4217.93m	2.149±0.047	4224.90m	2.369±0.079	4214.63m	4.249±0.123	4216.68m	6.325±0.200	4214.84m	1.500±0.139
4218.95m	2.253±0.050	4226.89m	2.566±0.084	4215.64m	4.041±0.117	4217.68m	6.218±0.199	4215.85m	1.309±0.122
4220.96m	2.265±0.050	4227.90m	2.395±0.079	4216.63m	4.169±0.121	4218.75m	5.753±0.184	4216.84m	1.348±0.125
4221.98m	2.331±0.052	4228.91m	2.519±0.083	4217.63m	4.128±0.120	4219.79m	5.699±0.181	4217.84m	1.305±0.121
4222.95m	2.251±0.050	4229.88m	2.618±0.086	4218.70m	4.037±0.117	4220.69m	5.870±0.188	4218.86m	1.126±0.105
4223.94m	2.234±0.049	4230.91m	2.639±0.087	4219.74m	3.914±0.113	4221.69m	5.930±0.189	4219.88m	0.881±0.082
4224.94m	2.212±0.049	4231.91m	2.538±0.083	4220.64m	3.961±0.115	4222.69m	6.144±0.196	4220.86m	0.987±0.092
4225.92m	2.246±0.050	4232.90m	2.512±0.083	4221.64m	3.899±0.113	4223.69m	6.466±0.207	4221.84m	0.845±0.078
4226.94m	2.314±0.051	4233.89m	2.516±0.083	4222.63m	4.025±0.117	4224.69m	6.518±0.209	4222.85m	0.957±0.088
4227.95m	2.303±0.051	4234.89m	2.386±0.079	4223.64m	4.311±0.125	4226.71m	6.145±0.195	4223.85m	1.087±0.101
4228.94m	2.256±0.050	4235.90m	2.610±0.086	4224.63m	4.467±0.130	4227.69m	6.234±0.199	4224.85m	0.976±0.091
4229.93m	2.291±0.051	4236.90m	2.655±0.088	4226.64m	4.022±0.117	4229.73m	6.050±0.192	4225.89m	1.084±0.101
4230.95m	2.313±0.051	4237.90m	2.517±0.083	4227.64m	4.001±0.116	4230.69m	6.079±0.194	4226.83m	1.122±0.104
4231.95m	2.108±0.046	4239.90m	2.627±0.087	4228.75m	4.069±0.118	4231.70m	6.181±0.196	4227.86m	1.160±0.108
4232.94m	2.214±0.049	4240.89m	2.547±0.084	4229.68m	3.858±0.112	4232.68m	6.254±0.200	4228.86m	1.010±0.094
4233.94m	2.169±0.048	4241.89m	2.561±0.084	4230.64m	3.888±0.113	4233.68m	6.371±0.201	4229.84m	1.027±0.095
4234.94m	2.074±0.045	4243.90m	2.561±0.084	4231.65m	3.847±0.111	4234.68m	6.398±0.204	4230.86m	1.192±0.111
4235.94m	2.164±0.048	4244.90m	2.584±0.085	4232.63m	3.912±0.113	4235.68m	6.395±0.204	4231.86m	1.009±0.094
4236.95m	2.234±0.049	4245.90m	2.527±0.083	4233.63m	3.889±0.113	4236.68m	6.522±0.208	4232.85m	0.890±0.083
4237.95m	2.176±0.048	4246.89m	2.565±0.084	4234.64m	3.855±0.111	4237.69m	6.256±0.200	4233.85m	1.070±0.100
4239.94m	2.164±0.048	4247.88m	2.609±0.086	4235.64m	3.856±0.111	4238.68m	6.196±0.197	4234.85m	0.997±0.092

Table 6—Continued

Mrk 290		Mrk 817		NGC 3227		NGC 3516		NGC 5548	
JD ^a	$F_{H\beta}^b$								
4240.93m	2.143±0.047	4248.89m	2.615±0.086	4236.63m	3.830±0.111	4239.70m	6.131±0.195	4235.85m	1.010±0.094
4241.93m	2.115±0.046	4249.89m	2.421±0.080	4237.64m	3.718±0.108	4240.68m	6.304±0.201	4236.85m	0.875±0.082
4242.94m	2.074±0.045	4250.89m	2.571±0.085	4238.63m	3.756±0.109	4241.68m	6.493±0.207	4237.85m	0.953±0.088
4243.95m	2.114±0.046	4251.89m	2.521±0.083	4239.66m	3.991±0.116	4242.70m	6.323±0.201	4239.85m	0.905±0.084
4244.94m	2.078±0.046	4252.88m	2.551±0.084	4240.63m	3.930±0.114	4243.69m	6.662±0.213	4240.84m	0.952±0.088
4245.95m	2.073±0.045	4253.89m	2.480±0.081	4241.63m	4.028±0.117	4244.75m	6.223±0.198	4241.84m	0.981±0.091
4246.94m	2.141±0.047	4254.85m	2.405±0.080	4242.64m	3.816±0.110	4245.69m	6.208±0.198	4242.92m	0.950±0.088
4247.93m	2.043±0.045	4255.86m	2.670±0.088	4243.64m	4.363±0.126	4246.69m	6.139±0.195	4243.85m	1.037±0.096
4248.94m	2.114±0.046	4256.87m	2.566±0.084	4244.68m	4.049±0.118	4247.69m	5.749±0.183	4244.85m	0.984±0.091
4250.94m	2.167±0.048	4258.88m	2.600±0.086	4245.65m	4.207±0.122	4248.69m	6.103±0.195	4245.85m	0.992±0.092
4252.93m	2.181±0.048	4259.89m	2.434±0.080	4246.64m	4.218±0.122	4249.69m	6.168±0.197	4246.85m	0.741±0.069
4253.94m	2.157±0.047	4260.89m	2.544±0.084	4247.65m	4.220±0.122	4250.69m	5.914±0.189	4247.84m	0.958±0.090
4254.90m	2.055±0.045	4261.89m	2.503±0.082	4248.64m	4.260±0.123	4251.69m	5.698±0.182	4248.85m	0.740±0.069
4255.91m	2.027±0.044	4263.86m	2.319±0.077	4249.64m	4.273±0.124	4252.69m	5.805±0.184	4249.85m	0.846±0.079
4256.91m	2.148±0.047	4264.86m	2.335±0.077	4250.64m	4.139±0.120	4253.68m	5.898±0.186	4250.84m	0.659±0.061
4257.94m	2.002±0.044	4265.44c	2.157±0.080	4251.64m	4.268±0.123	4255.71m	5.973±0.190	4251.84m	0.615±0.057
4258.93m	2.005±0.044	4265.88m	2.346±0.078	4252.64m	4.034±0.117	4257.69m	5.576±0.178	4252.84m	0.801±0.074
4259.94m	1.928±0.043	4266.44c	2.326±0.086	4253.65m	3.873±0.112	4258.71m	6.062±0.193	4253.84m	0.827±0.077
4260.94m	2.033±0.044	4266.86m	2.341±0.078	4255.67m	3.695±0.107	4259.70m	5.887±0.185	4254.81m	0.870±0.081
4261.93m	1.908±0.042	4267.42c	2.392±0.089	4256.66m	3.857±0.112	4260.71m	5.631±0.178	4255.82m	1.070±0.100
4262.84d	1.915±0.060	4267.86m	2.360±0.078	4257.64m	3.473±0.101	4261.69m	5.493±0.174	4256.82m	0.988±0.092
4263.91m	1.920±0.043	4268.48c	2.435±0.090	4259.65m	3.872±0.112	4262.69m	5.194±0.163	4257.81m	1.093±0.101
4264.92m	1.856±0.041	4268.85m	2.447±0.080	4260.66m	3.476±0.101	4263.68m	5.431±0.171	4258.83m	1.028±0.096
4265.93m	1.818±0.040	4269.85m	2.338±0.077	4261.65m	3.537±0.103	4264.70m	5.417±0.173	4259.84m	1.174±0.109
4266.48c	1.820±0.061	4270.47c	2.234±0.082	4262.65m	3.183±0.092	4265.72m	5.004±0.156	4260.84m	0.984±0.091
4266.91m	1.845±0.041	4271.42c	2.105±0.078	4264.65m	3.394±0.098	4266.36c	5.213±0.369	4261.84m	1.306±0.121
4267.44c	1.887±0.062	4272.45c	2.254±0.083	4265.67m	3.471±0.100	4266.69m	5.238±0.165	4262.80m	1.200±0.112
4267.91d	1.894±0.042	4273.42c	2.166±0.080	4266.65m	3.519±0.102	4267.69m	5.161±0.163	4263.81m	1.121±0.104
4267.91m	1.770±0.055	4274.48c	2.170±0.080	4267.64m	3.661±0.106	4268.34c	4.934±0.349	4264.82m	1.089±0.101
4268.90m	1.876±0.042	4276.40c	2.082±0.077	4268.64m	3.892±0.113	4268.69m	5.101±0.160	4265.38c	1.253±0.120
4269.46c	1.866±0.062	4277.39c	2.067±0.077			4269.29c	5.047±0.357	4265.81m	1.114±0.104
4269.87d	1.894±0.060	4278.42c	2.182±0.080			4269.69m	4.768±0.149	4266.41c	0.987±0.094
4270.85d	1.805±0.057	4281.48c	2.148±0.080			4271.37c	4.018±0.284	4266.82m	1.095±0.101
4273.45c	1.865±0.062	4282.50c	2.185±0.080			4272.38c	3.586±0.254	4267.39c	1.275±0.121
4274.44c	1.859±0.062	4283.39c	2.387±0.088			4273.36c	3.521±0.249	4267.81m	1.277±0.118
4277.43c	1.982±0.066	4284.38c	2.288±0.084			4274.33c	3.911±0.277	4268.36c	1.248±0.118
4277.89d	1.942±0.061	4290.41c	2.211±0.081			4277.34c	3.974±0.281	4269.40c	1.088±0.104
4278.46c	1.893±0.062	4291.38c	2.159±0.080			4278.32c	4.500±0.319	4271.39c	1.067±0.101
4282.46c	1.872±0.062	4297.43c	2.180±0.080			4279.29c	3.776±0.267	4272.41c	1.006±0.096
4282.81d	2.008±0.063	4298.45c	2.324±0.086			4280.29c	3.619±0.256	4273.38c	1.039±0.099
4283.42c	1.943±0.064	4299.38c	2.219±0.082			4281.42c	3.889±0.275	4274.35c	1.072±0.101
4284.41c	1.974±0.065	4300.36c	2.266±0.084			4283.29c	3.902±0.276	4276.84d	1.059±0.082
4285.86d	1.950±0.062	4301.43c	2.256±0.083			4284.33c	4.070±0.288	4277.36c	1.147±0.109
4286.86d	2.093±0.066					4290.28c	4.150±0.294	4277.80d	1.040±0.081
4287.86d	2.041±0.064					4291.32c	3.658±0.259	4278.39c	1.031±0.098

Table 6—Continued

Mrk 290		Mrk 817	NGC 3227	NGC 3516		NGC 5548	
JD ^a	$F_{H\beta}$ ^b						
4288.86d	2.061±0.065			4296.31c	3.823±0.271	4278.83d	1.078±0.083
4289.42c	2.071±0.069			4299.33c	3.655±0.259	4282.76d	1.161±0.090
4290.44c	1.935±0.064			4300.30c	3.441±0.244	4283.35c	1.223±0.116
4290.85d	2.134±0.067					4284.35c	0.933±0.088
4291.41c	2.092±0.070					4285.77d	1.109±0.086
4296.42c	1.977±0.066					4286.76d	0.919±0.070
4297.48c	1.985±0.066					4287.76d	0.926±0.071
4298.42c	1.868±0.062					4288.76d	1.017±0.078
4300.40c	1.977±0.065					4289.34c	1.058±0.100
4301.46c	2.001±0.066					4290.38c	1.085±0.103
						4290.75d	1.153±0.088
						4291.35c	1.118±0.107
						4292.84d	1.101±0.084
						4293.77d	1.143±0.088
						4296.33c	1.215±0.116
						4299.35c	1.286±0.122
						4300.32c	1.251±0.118
						4301.38c	1.277±0.121

^aJulian Dates are -2450000 and include the same observatory codes as Table 5.

^b $H\beta$ flux is in units of 10^{-13} ergs s^{-1} cm^{-2} .

Table 7. Light Curve Statistics

Objects	Continuum Statistics					$H\beta$ Line Statistics				
	Sampling(days)		Mean			Sampling(days)		Mean		
	$\langle T \rangle$	T_{median}	Flux ^a	F_{var}	R_{max}	$\langle T \rangle$	T_{median}	Flux ^b	F_{var}	R_{max}
(1)	(2)	(3)	(4)	(5)	(6)	(7)	(8)	(9)	(10)	(11)
Mrk 290	0.77	0.52	0.94	0.18	2.18 ± 0.17	1.18	1.00	2.09	0.07	1.32 ± 0.05
Mrk 817	0.84	0.56	5.06	0.05	1.27 ± 0.03	1.33	1.00	2.41	0.05	1.29 ± 0.06
NGC 3227	0.55	0.45	3.27	0.10	1.88 ± 0.09	1.13	1.00	3.99	0.08	1.48 ± 0.06
NGC 3516	0.60	0.54	4.86	0.28	5.90 ± 1.50	1.26	1.00	5.54	0.15	1.94 ± 0.15
NGC 4051	0.56	0.45	4.49	0.09	1.69 ± 0.11	1.08	1.00	4.67	0.07	1.39 ± 0.07
NGC 5548	0.70	0.48	2.29	0.11	1.71 ± 0.06	1.09	1.00	1.20	0.26	3.74 ± 0.49

^aFluxes are the same units as Table 5.

^bFluxes are the same units as Table 6.

Table 8. Rest Frame Lags, Line Widths, Black Hole Masses, and Luminosities

Objects	r_{\max}	τ_{cent} (days)	τ_{peak} (days)	σ_{line} (km/s)	FWHM (km/s)	M_{vir} ($\times 10^6 M_{\odot}$)	M_{BH}^{a} ($\times 10^6 M_{\odot}$)	$\log L_{5100}$ (ergs s $^{-1}$)
(1)	(2)	(3)	(4)	(5)	(6)	(7)	(8)	(9)
Mrk 290	0.632	$8.72^{+1.21}_{-1.02}$	$9.2^{+1.5}_{-1.4}$	1609 ± 47	4270 ± 157	$4.42^{+0.67}_{-0.67}$	$24.3^{+3.7}_{-3.7}$	$43.00^{+0.08}_{-0.08}$
Mrk 817 ^b	0.614	$14.04^{+3.41}_{-3.47}$	$16.0^{+3.9}_{-5.3}$	2025 ± 5	5627 ± 30	$11.3^{+2.7}_{-2.8}$	$43.3^{+10.5}_{-10.7}$	$43.78^{+0.02}_{-0.02}$
NGC 3227	0.547	$3.75^{+0.76}_{-0.82}$	$2.99^{+2.00}_{-1.00}$	1376 ± 44	3578 ± 83	$1.39^{+0.29}_{-0.31}$	$7.63^{+1.62}_{-1.72}$	$42.11^{+0.04}_{-0.04}$
NGC 3516	0.894	$11.68^{+1.02}_{-1.53}$	$7.43^{+1.99}_{-0.99}$	1591 ± 10	5175 ± 96	$5.76^{+0.51}_{-0.76}$	$31.7^{+2.8}_{-4.2}$	$43.17^{+0.15}_{-0.15}$
NGC 4051	0.583	$1.87^{+0.54}_{-0.50}$	$2.60^{+0.79}_{-1.40}$	927 ± 64	1034 ± 41	$0.31^{+0.10}_{-0.09}$	$1.73^{+0.55}_{-0.52}$	$41.82^{+0.10}_{-0.36}$
NGC 5548	0.708	$12.40^{+2.74}_{-3.85}$	$6.1^{+9.4}_{-2.8}$	1822 ± 35	4849 ± 112	$8.04^{+1.80}_{-2.51}$	$44.2^{+9.9}_{-13.8}$	$42.91^{+0.05}_{-0.05}$

^aUsing Onken et al. (2004) calibration (except Mrk 817, see below).

^bThe weak and poorly defined, triple-peaked profile of the H β emission in the rms spectrum necessitated the use of the line width measured from the mean spectrum for Mrk 817 (Columns 5 and 6) and a black hole mass (Column 8) calculated with the scale factor determined by Collin et al. (2006) for the use of this line width measurement, $f = 3.85$, instead of the standard Onken et al. (2004) value of $f = 5.5$ that was used for all other objects.

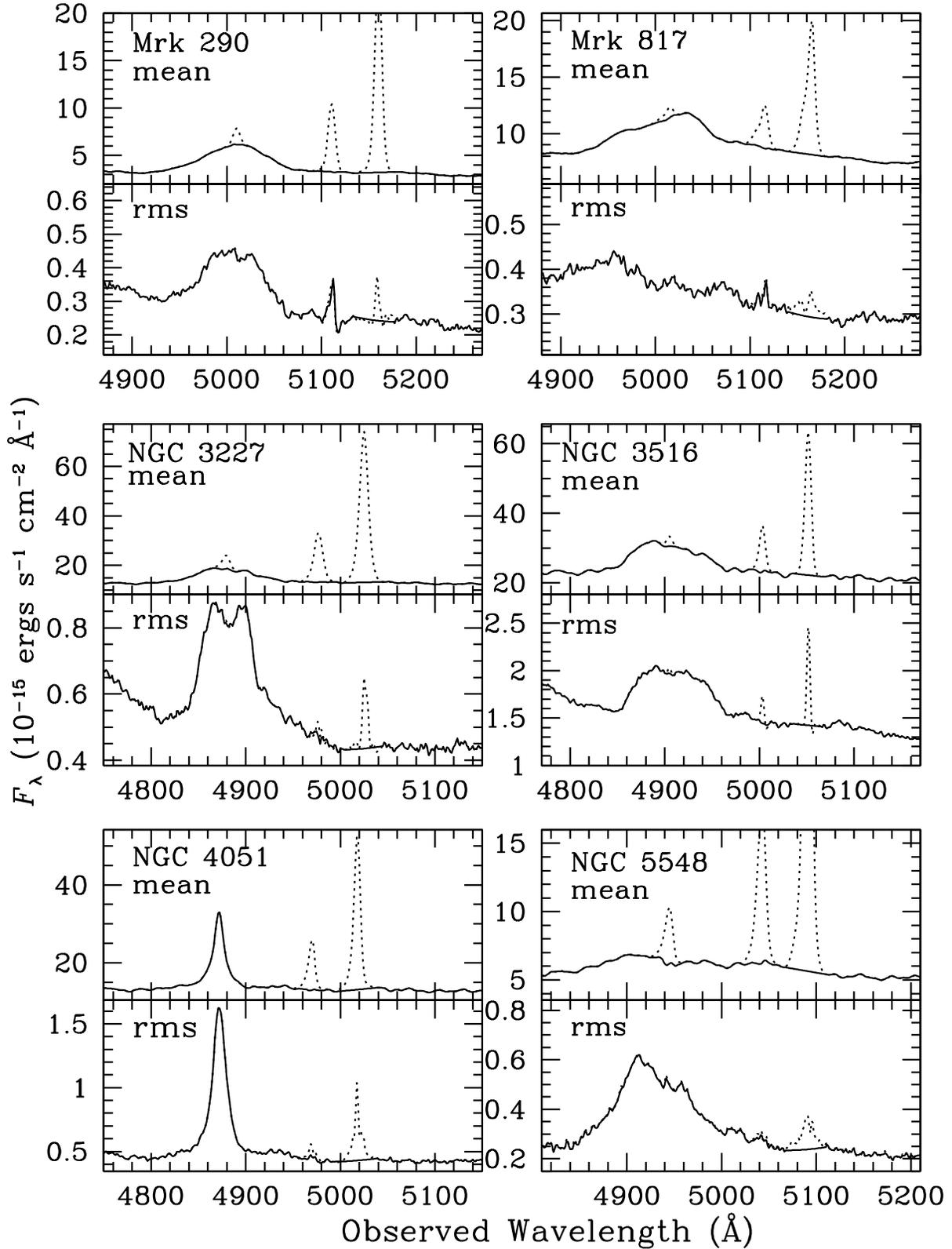


Fig. 1.—: Mean and rms (variable emission) spectra from MDM observations. The solid lines show the narrow-line subtracted spectra, while the dotted lines show the narrow-line component of $\text{H}\beta$ and the $[\text{O III}] \lambda\lambda 4959, 5007$ narrow emission lines and rms residuals.

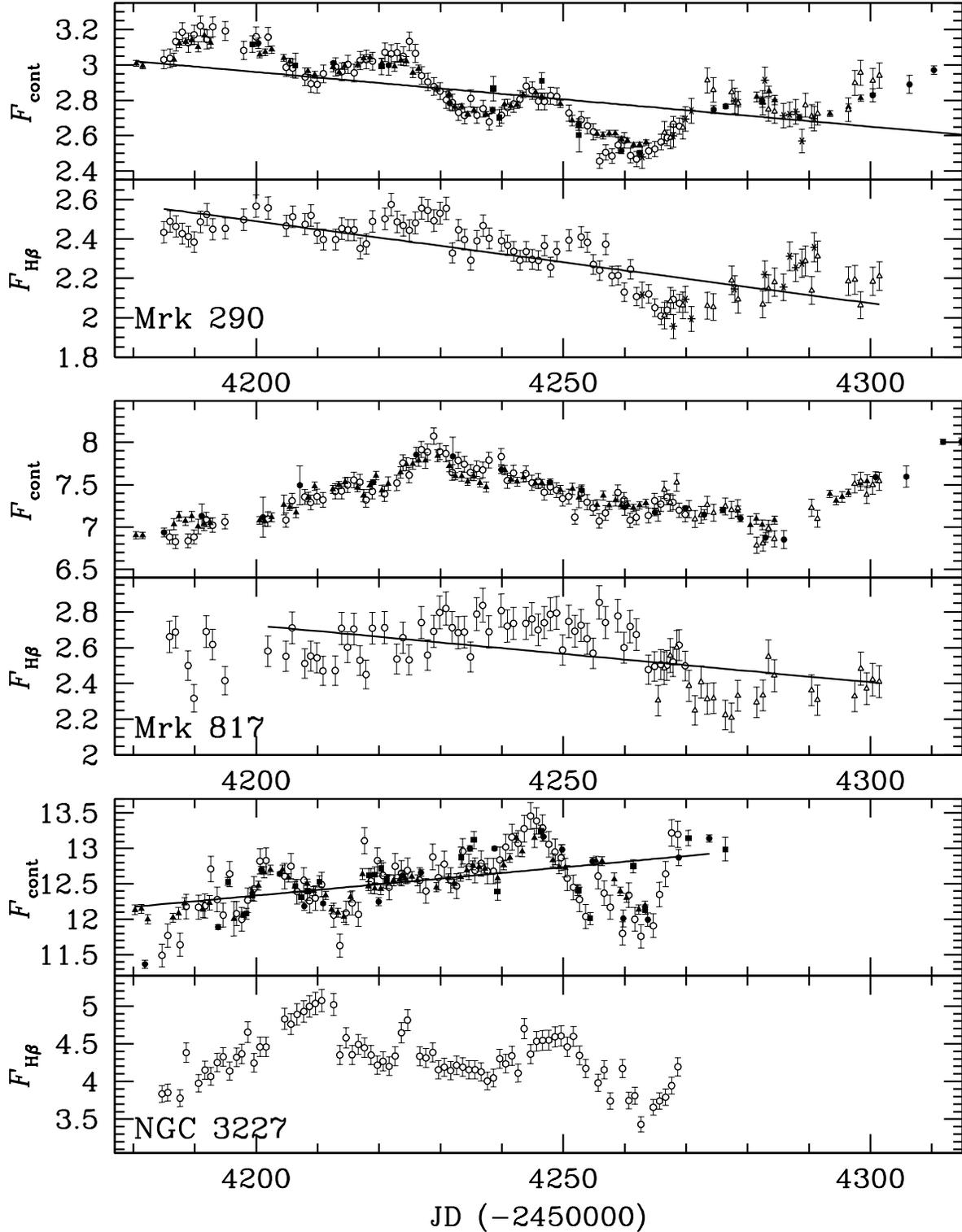


Fig. 2.—: Light curves showing complete set of observations from all sources for all objects. *Top:* The 5100 Å continuum flux in units of 10^{-15} ergs s^{-1} cm^{-2} Å $^{-1}$. *Bottom:* H β λ 4861 line flux in units of 10^{-13} ergs s^{-1} cm^{-2} . Observations from different sources are as follows: CrAO photometry — solid triangles, MAGNUM photometry — solid circles, UNEbr. photometry — solid squares, MDM spectroscopy — open circles, CrAO spectroscopy — open triangles, and DAO spectroscopy — asterisks. The solid lines show linear, secular-variation detrending fits to the light curves.

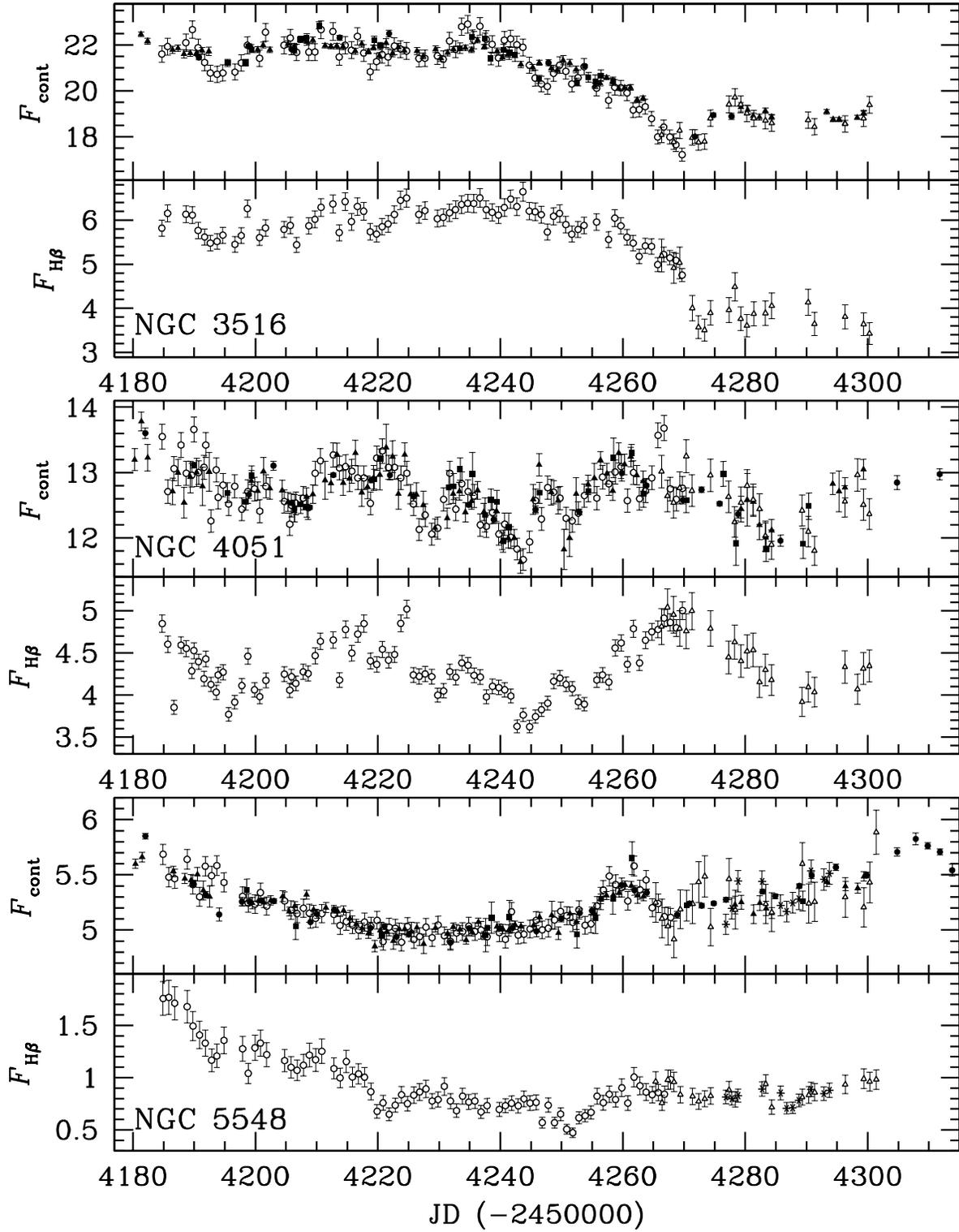


Fig. 2.— *Continued.*

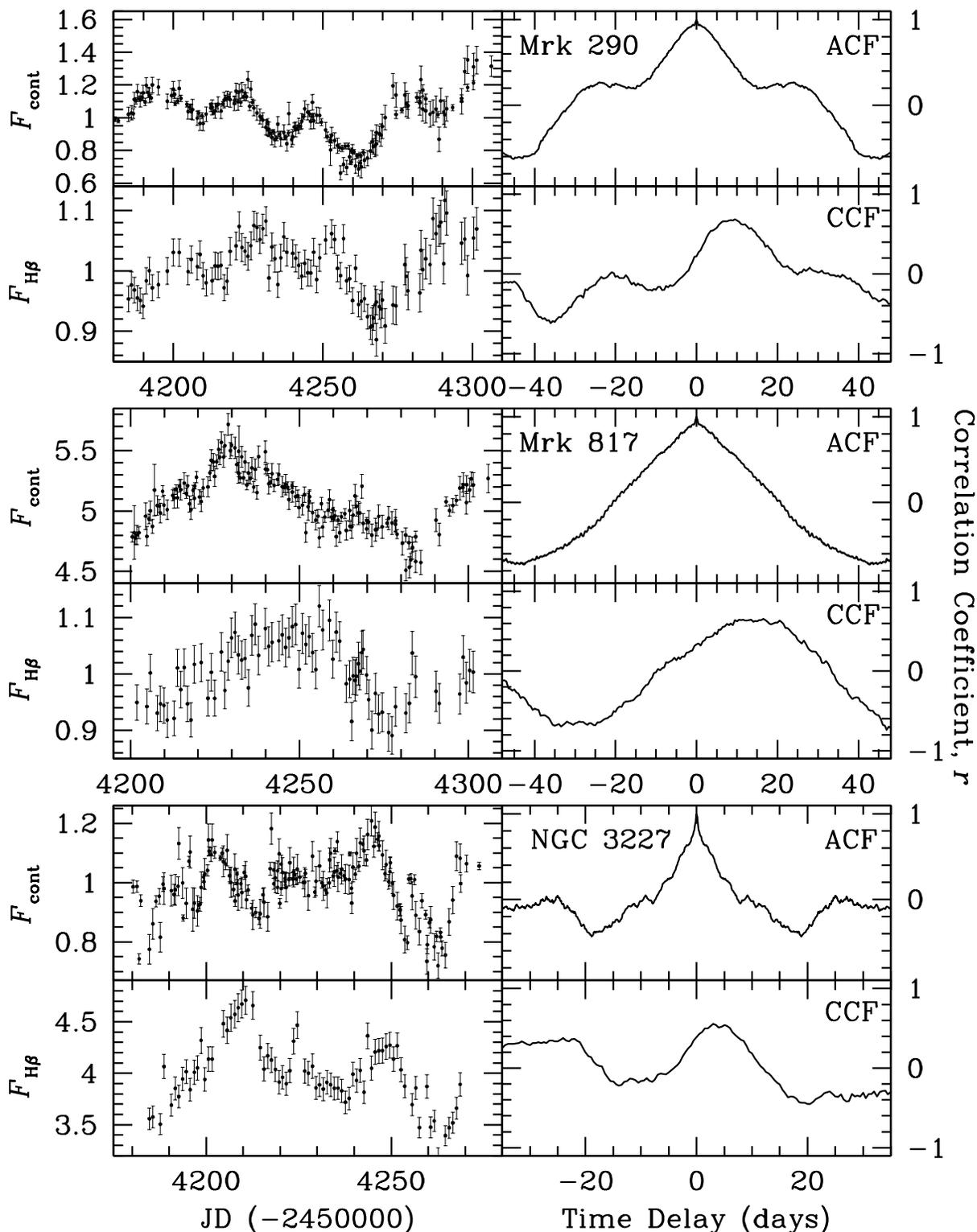


Fig. 3.— *Left panels:* Merged and detrended (where applicable) continuum (top) and H β (bottom) light curves used for cross correlation analysis. Units are the same as Tables 5 and 6, but the flux scale of each detrended light curve is arbitrary. *Right panels:* Cross-correlation functions for the light curves. Each top panel shows the autocorrelation function of each continuum light curve, and the bottom panels show the cross-correlation function of H β with the continuum.

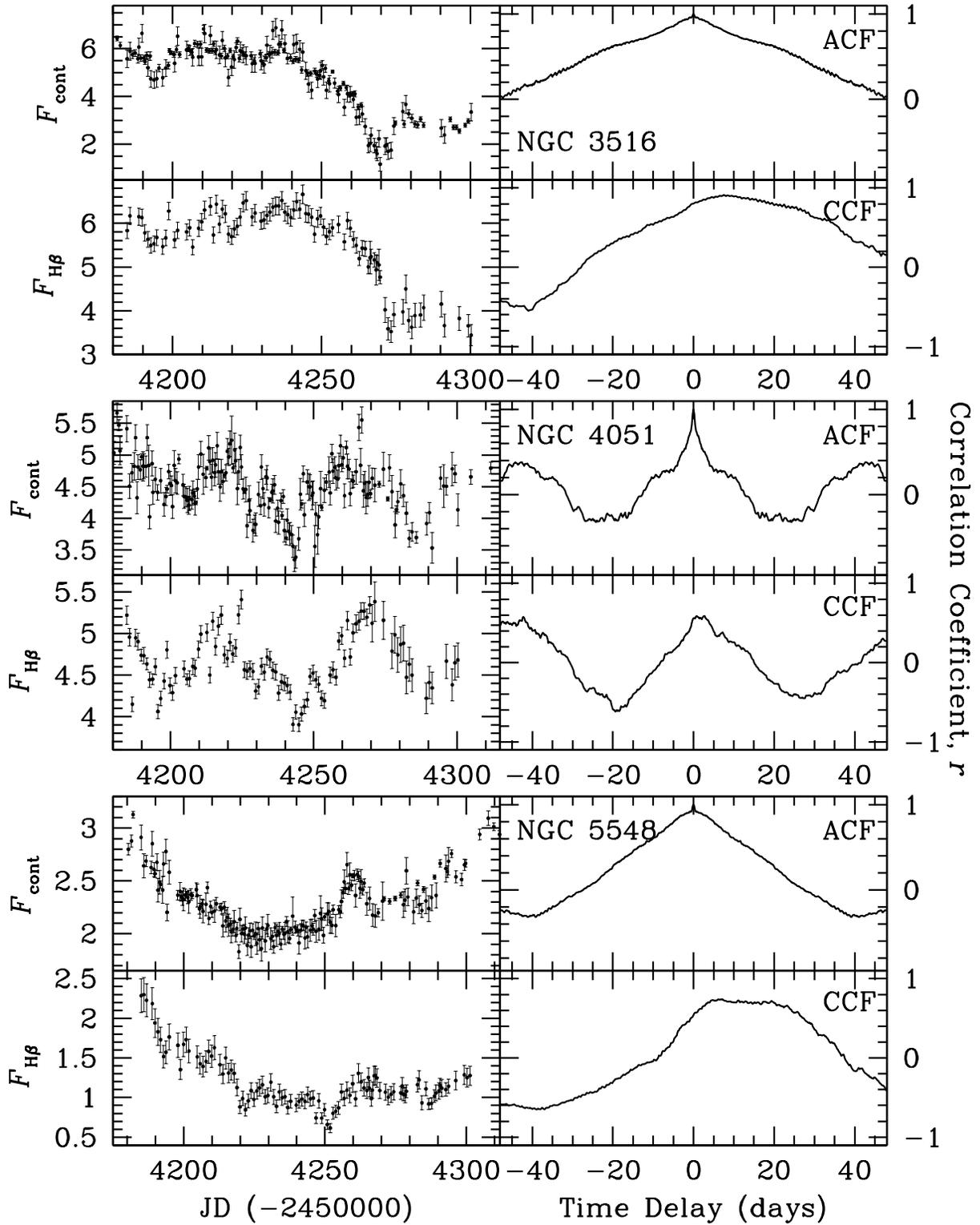


Fig. 3.— *Continued.*

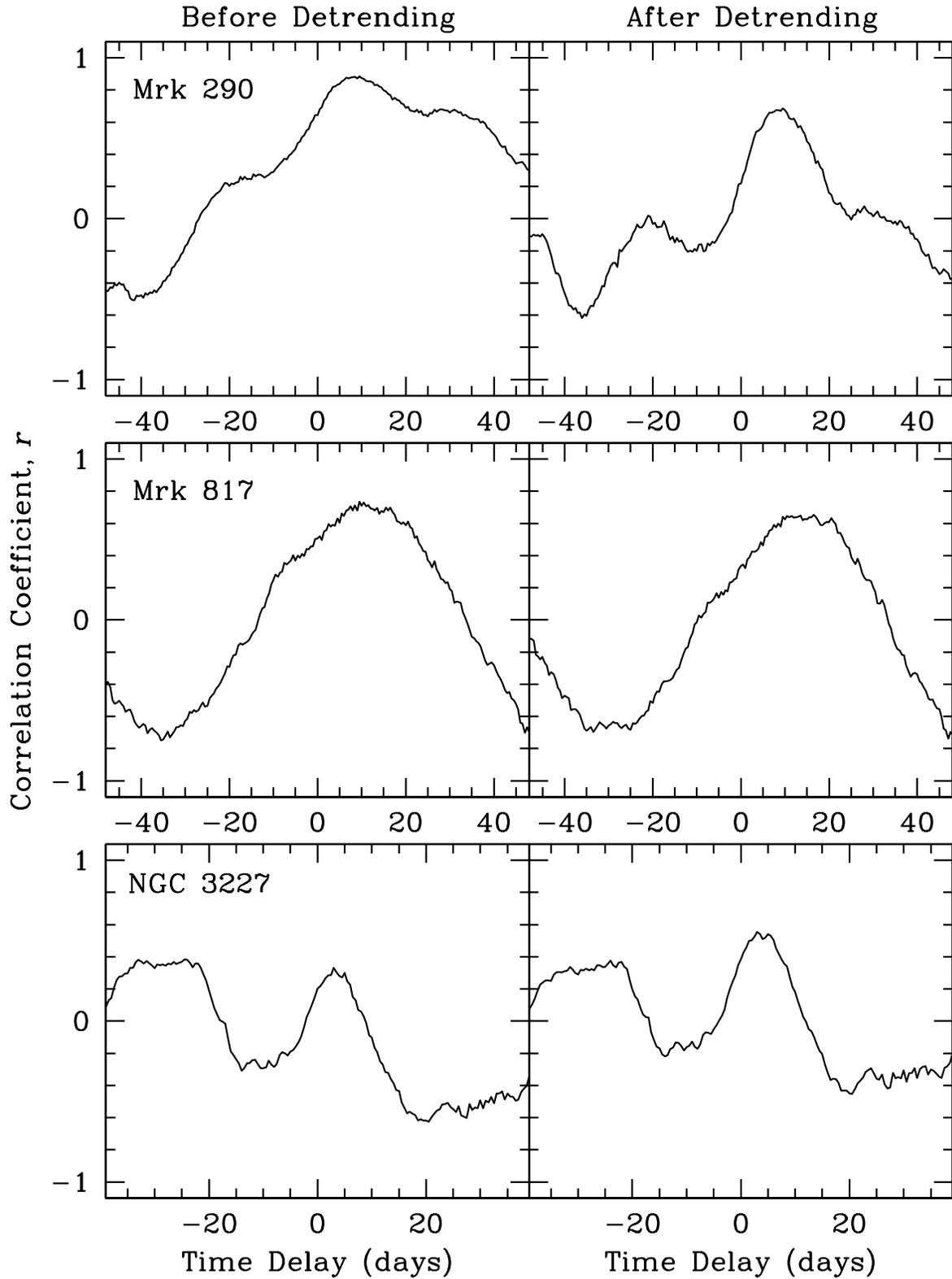


Fig. 4.— CCFs before (left) and after (right) detrending selected light curves of Mrk 290 (top), Mrk 817 (middle), and NGC 3227 (bottom). See Section 2.4 for details.

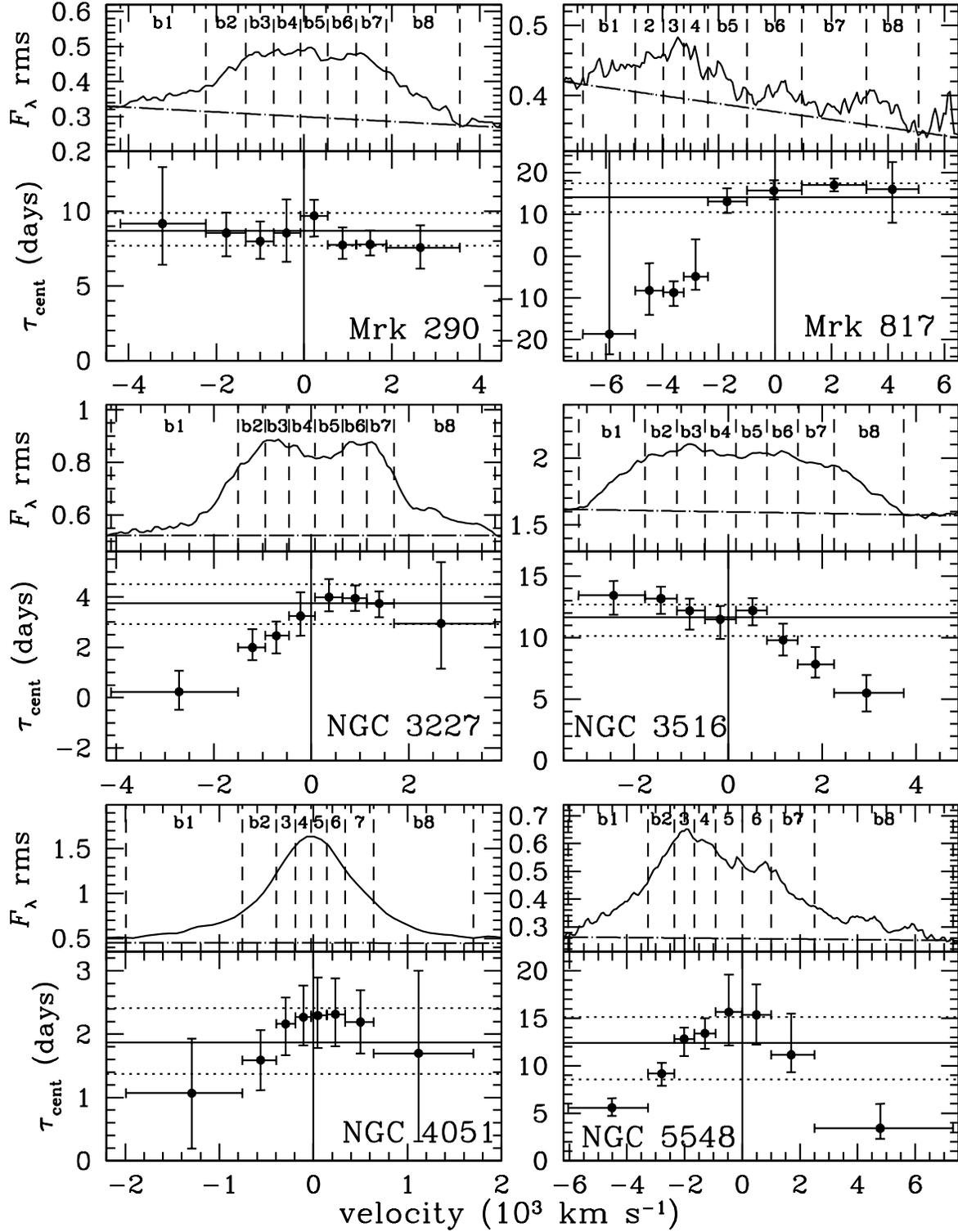


Fig. 5.— *Top panels:* H β rms spectral profile of each object broken into bins of equal flux (numbered and separated by dashed lines) with the linearly-fit continuum level shown (dotted-dashed line). Flux units are the same as in Fig. 1. *Bottom panels:* Velocity-resolved time-delay measurements. Time delay measurements and errors are determined similarly to those for the mean BLR lag, and error bars in the velocity direction show the bin size. The horizontal solid and dotted lines show the mean BLR centroid lag and associated errors, calculated in Section 2.4.

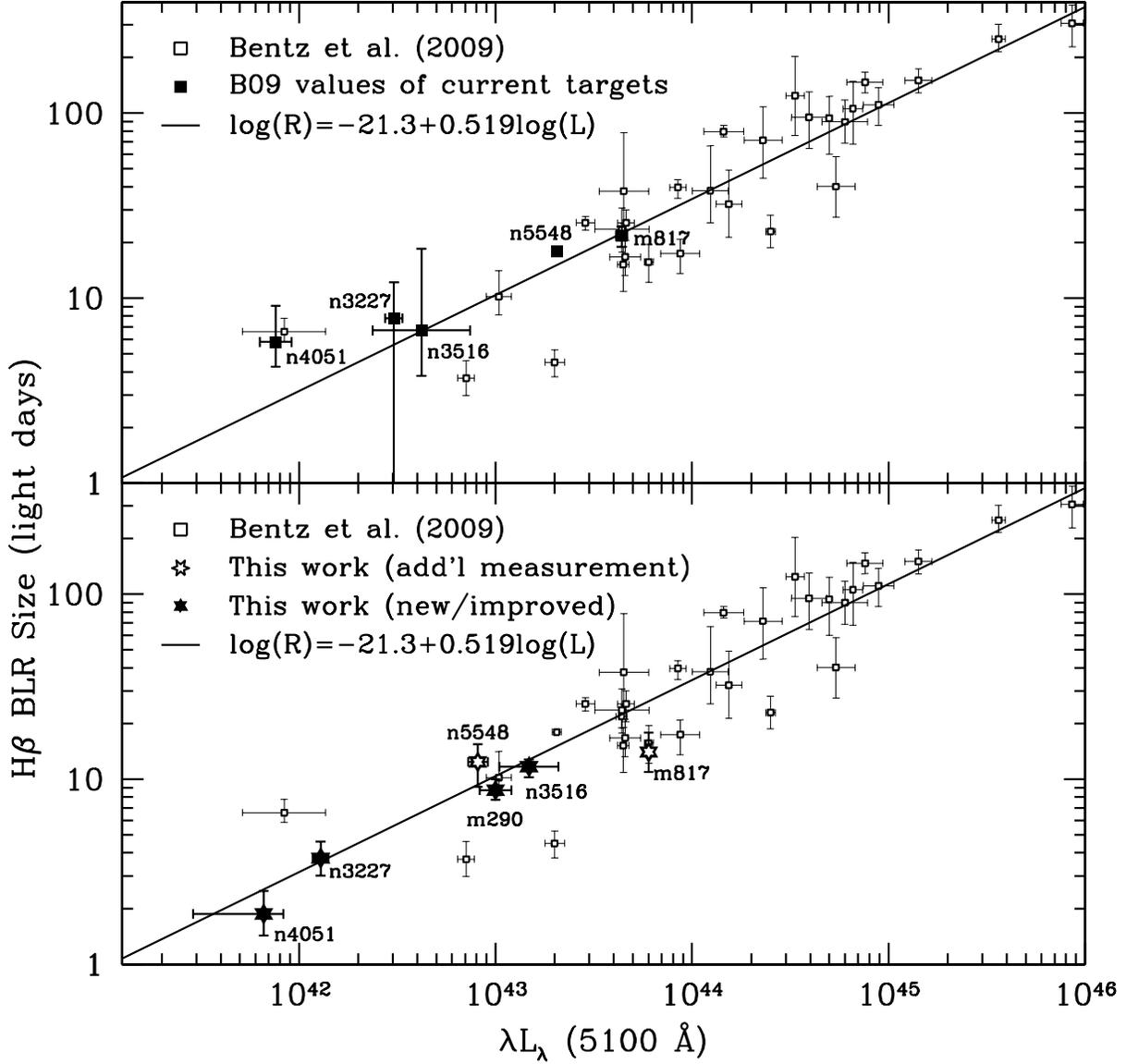


Fig. 6.— *Top:* Most recently calibrated $R_{\text{BLR}}-L$ relation (Bentz et al. 2009b, solid line). The closed points show the location of our targets, and open points show all other objects used by Bentz et al. *Bottom:* Same as top but with our new results displayed. Solid stars show new objects or improvements upon past results which replace solid points of NGC 4051, NGC 3227, NGC 3516, and Mrk 290 in top panel, and open points show results for NGC 5548 and Mrk 817, which serve as additional measurements for these objects but do not replace previous measurements. Note that we keep the same calibration of the relationship as determined by Bentz. et al.; no new fit has been calculated with our new results.

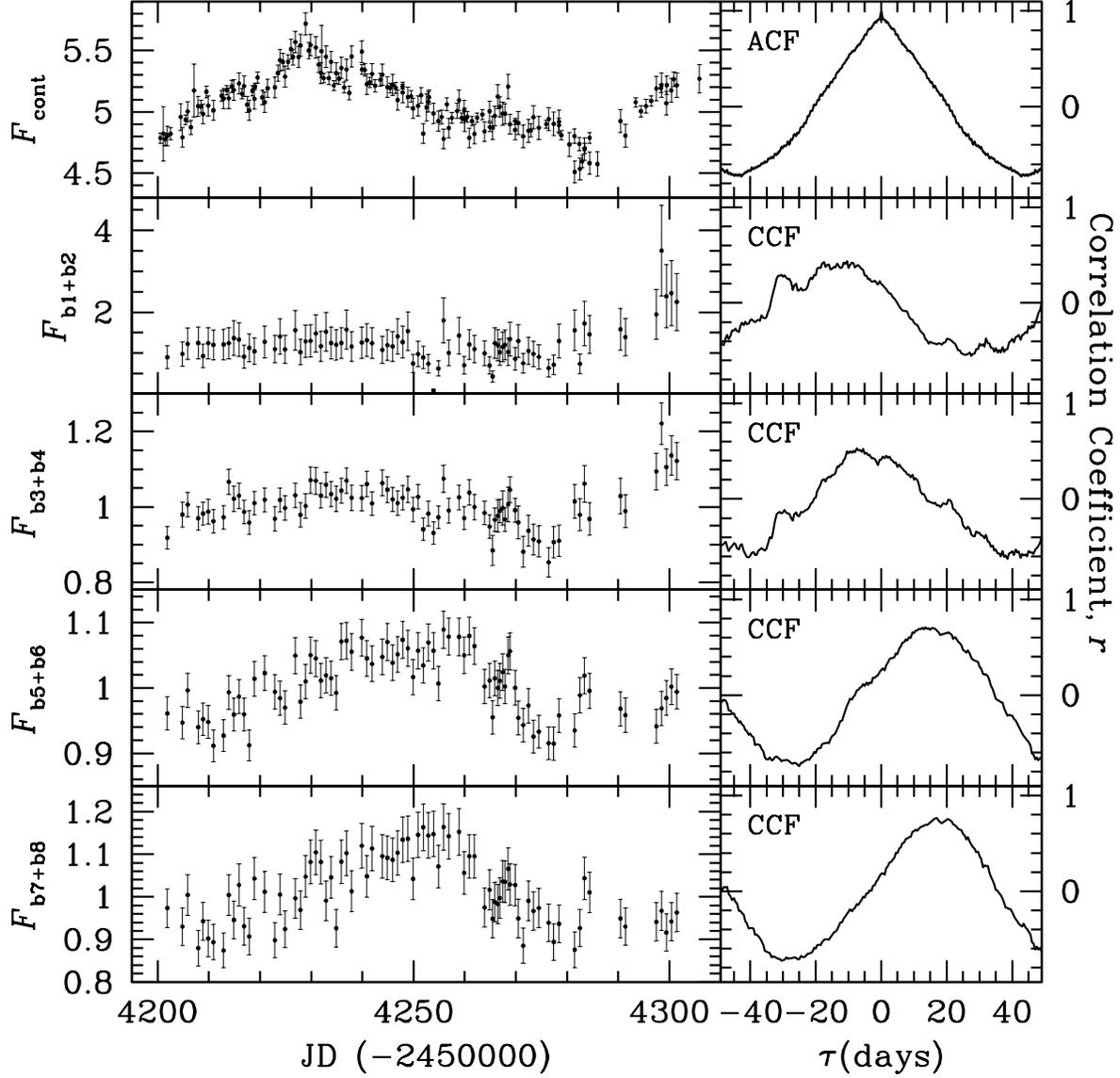


Fig. 7.— *Left panels:* Continuum (top) and linearly detrended $H\beta$ light curves of Mrk 817 from four equal flux bins. Units are the same as Tables 5 and 6. *Right panels:* Cross-correlation functions for the light curves. The top panel shows the autocorrelation function of the continuum light curve, and the lower panels show the cross-correlation function of each $H\beta$ bin with the continuum.